

DETECTION OF SHORT CO₂ LASER PULSES

DETECTION
OF
SHORT CO₂ LASER PULSES

By

DANIEL FERNAND ROLLIN, B.Sc.

A Thesis

Submitted to the School of Graduate Studies
in Partial Fulfilment of the Requirements
for the Degree
Master of Engineering

McMaster University

November 1974

DETECTION
OF
SHORT CO₂ LASER PULSES

by

DANIEL FERNAND ROLLIN, B.Sc.

PART A: MCMASTER (OFF-CAMPUS) PROJECT*

A Report Submitted to the School of Graduate Studies
in Partial Fulfilment of the Requirements
for the Degree
Master of Engineering

Department of Engineering Physics
McMaster University
Hamilton, Ontario, Canada.

November 1974

* One of two project reports: The other part is designated PART B:
ON-CAMPUS PROJECT.

MASTER OF ENGINEERING (1974)
(Engineering Physics)

McMASTER UNIVERSITY
Hamilton Ontario.

TITLE: Detection of Short CO₂ Pulses

AUTHOR: Daniel Fernand Rollin, B.Sc. (University of Ottawa)

SUPERVISORS: Dr. B. Garside and Dr. J. Alcock

NUMBER OF PAGES: vii 21

ABSTRACT

A passively mode-locked multi-atmosphere CO₂ laser was used to produce sub-nanosecond pulses. After up-conversion of the 10.6 um radiation in a proustite crystal detection was done with a streak camera-optical multichannel analyser combination. Pulses shorter than 100 psec (FWHM) were recorded.

ACKNOWLEDGEMENTS

I wish to express my gratitude to Drs A. J. Alcock and B. Garside for their assistance in arranging my stay as a cooperative student at N.R.C. Thanks are also due Dr A.C. Walker for his guidance throughout the course of this work.

The National Research Council of Canada is thanked for its financial assistance in the form of a fellowship.

TABLE OF CONTENTS

Abstract	iii	
Acknowledgements	iv	
List of Figures	vi	
List of Tables	vii	
INTRODUCTION	1	
CHAPTER II	Description of the Apparatus	2
2.1	Introduction	2
2.2	CO ₂ Laser	2
2.3	Nd:Yag Laser	3
2.4	Up-conversion Process	3
2.5	The Streak Camera-OMA Detection System	5
2.6	Experimental Results using 4 nsec/cm Streak Velocity	8
CHAPTER III	Low Light Level Fast Sweep Measurements	9
3.1	Measurements with 1 nsec/cm Streak Velocity	9
3.2	Low Light Level Detection	9
CONCLUSION		11
BIBLIOGRAPHY		12

LIST OF FIGURES

FIGURE		Page
1	SCHEMATIC DIAGRAM OF EXPERIMENTAL ARRANGEMENT	16
2	a) DIAGRAM OF PREIONIZER AND MAIN DISCHARGE CIRCUITS	
	b) CROSS SECTION OF LASER DISCHARGE CHAMBER	17
3	MODE-LOCKED AND Q-SWITCHED Nd:Yag LASER	18
4	RECORDING OF AN INTENSITY LIMITED Nd:Yag PULSE	19
5	EXPERIMENTAL ARRANGEMENT FOR THE DETECTION OF UP-CONVERTED CO ₂ LASER PULSES	20
6	DISPLAY OF AN INTENSITY LIMITED Nd:Yag PULSE	21
7	DISPLAY OF A CO ₂ PULSE	22

LIST OF TABLES

TABLE		Page
I	CHARACTERISTICS OF THE HIGH PRESSURE CO ₂ LASER	13
II	CHARACTERISTICS OF p-TYPE Ge ETALONS	14
III	CHARACTERISTICS OF THE IMAGE CONVERTER TUBE	15

1 - INTRODUCTION

The work done by Drs. A.J. Alcock and A. Walker (N.R.C., Ottawa) has been carried out on two aspects: the production of subnanosecond pulses from a mode-locked high pressure CO_2 laser and the detection of these pulses using frequency up-conversion techniques.

This report will describe:

In Chapter II, the experimental set up built by Alcock and Walker followed by a short summary of the first results obtained.

In Chapter III, the further improvements made to the system and the results obtained since the author joined the group.

CHAPTER II

DESCRIPTION OF THE APPARATUS

2.1 INTRODUCTION

An over simplified schematic of the experimental set up is shown on Figure 1. The high intensity 10.6 μm CO_2 output and the smoothed and stretched pulses from a Nd:Yag laser are incident on a proustite crystal. Phase matching results in the production of sum-frequency radiation at 0.96 μm . A detection system comprising an optical multi-channel analyser (OMA) coupled into a streak camera is described.

2.2 CO_2 LASER

The high pressure CO_2 laser has been described in the literature (Reference : 1 , 2 , 3...). It consists of a pressure chamber containing a pair of stainless steel electrodes 26 cm long and 0.7 cm apart. On each side, two rows of 13 tungsten rod electrodes 1 to 2 mm apart from each other provide a preionizing discharge. Clock diagram of the discharge circuit is shown on Figure 2. The main discharge comes from a 5-stage Marx bank. The preionizer is energized by a single 0.05 μF capacitor. Preionizer electrodes are coupled to this capacitor through 250 pF capacitors which control the sequenced discharges. Relevant figures concerning the specifications and operation of the laser are given in Table I.

The laser is mode locked using a 2 mm thick slab of 1.0cm P -type Ge placed at Brewster's angle and a 2 mm thick p -type Ge

etalon. The characteristics of the etalon are listed in Table II. It should be noticed that the etalon limits the band width of the output since the bandwidth of the pressure broadened CO₂ rotational line was estimated to be 3.5 GHz/atm (Reference 3)

2.3 Nd:Yag LASER

The Nd:Yag laser is used in two ways: Q-switched with intensity limiters for interaction together with the 10.6 um radiation in the proustite, and mode locked for calibration of the streak camera. Figure 3 shows the set up in each case.

For mode locked operation, the configuration is that described by Clobes & Brienza (Ref. 6) who observed 20 psec pulses. The dye was Kodak 9740 at a concentration of 3.5% (volumetric) in chlorobenzene. The dye cell was 2.5 mm thick and placed at Brewster's angle near the output mirror. For preliminary check the output was detected with a fast Si PIN photodiode feeding a Tektronix 519 oscilloscope having a 1 GHz bandwidth.

For Q-switched operation, two 2 mm thick slabs of Ga As, placed at Brewster's angle, were used to limit the pulse intensity and smooth it (see Reference: 7, 8, 12). The Q switch was a 1-meter concave mirror rotating at 400 cps. A typical pulse photographed with the 519 scope is shown on Figure 4. Typical intensity is 400 W/cm².

2.4 UP-CONVERSION PROCESS

a) INTRODUCTION AND THEORY.

The frequency up-conversion is achieved in a proustite crystal. The theory of frequency interaction in birefringent materials has been reviewed by Midwinter & Warner (9) and Armstrong et al (4). The conditions for phase matching are:

$$\mathbf{v}_3 = \mathbf{v}_1 + \mathbf{v}_2$$

$$\vec{k}_3 = \vec{k}_1 + \vec{k}_2 - \vec{\Delta k}$$

where Δk must be nul. Subscript 1 and 2 refers to the CO₂ 10.6 um radiation and to the Nd:Yag 1.06 um radiation. Subscript 3 applies to the up-converted .96 um. Phase matching is type II in a negative uniaxial crystal and intensity in the .96 um radiation is given by

$$I_3(d) = \frac{w_3}{w_2} I_2 \sin^2 \left(\frac{\pi d}{l} \right)$$

Where d is the distance traveled in the crystal and I₂ the 1.06 um intensity before entering the crystal.

$$\frac{I_3}{I_2} = (8\pi)^{3/2} \left(\frac{10^7}{c} \right)^{1/2} (\lambda_2 \lambda_3 n_1 n_2 n_3)^{-1/2}$$

$$d \text{ eff } (I_1)^{1/2}$$

with $d \text{ eff} = d_{22} \cos^2 \theta_m$ (esu)

c velocity of light in cm/sec

n refractive index

A linear relation is approached when $\frac{\pi d}{\lambda}$ is small:

$$I_3 = \frac{5.67 \times 10^9 d^2 d_{\text{eff}}^2 I_1 I_2}{n_1 n_2 n_3}$$

It should be noticed that the above equations are valid in the case where $I_1 \gg I_2$.

2.5 STREAK CAMERA/OMA DETECTION SYSTEM.

Although the fast photodiode described in section 2.3 is sensitive to the .96 um light, it exhibits, together with the Tecktronix 519, a bandwidth of only 1 GHz. Furthermore, as reported by Alcock and Walker (Reference 2) a tailing effect due to the photodiode decreases the capabilities of this detection system. It was replaced by an image converter streak camera having a S-1 photocathode. The operation of this streak camera was described by Schelev et al (Reference 10 11) and a similar instrument was described by Bradley et al (Reference 5). Table III gives the characteristics and performance of the commercial model used. Special attention is given to the resolution which is limited by:

- i) The spatial resolution (line pairs/mm)

The equivalent line resolution limit is

$$\tau_s = \frac{1}{v \delta}$$

where v is the streak velocity (mm/sec). The static spatial resolution can be found by viewing a conventional target with the

camera used as an image converter (no ramp voltage applied).

However many phenomena limits the dynamic spatial resolution,

mainly space charge effects and over loading of the photocathode.

To keep a spatial resolution of at least 10 lp/mm the maximum

current density was estimated to be 0.1 A/cm^2 (Schelev, Reference

11).

ii) The total transit time spread τ_2 which results from the energy distribution of the electrons leaving the photocathode.

If we suppose that the electrons leave the cathode with a velocity

$$v_0 \pm \Delta v/2$$

and since

$$v_0 \ll v_f = \sqrt{\frac{2El_e}{m}}$$

where v_f mean velocity of electrons at the anode

E electric field

l length of the tube

m electronic mass

Then in a final approximation v_0 can be neglected and

$$\begin{aligned} \tau_2 &= \Delta t_+ - \Delta t_- \\ &= \sqrt{\frac{2m}{l^2}} \left[\frac{(\Delta E)^{1/2}}{E} \right] \end{aligned}$$

Δt_+ , Δt_- : transit time of electrons having initial velocities

$$v_0 + \Delta v/2 \quad \text{and} \quad v_0 - \Delta v/2$$

ΔE energy spread of electrons at the photocathode

For 1 μm this is approximately 0.3 eV. This value,

compared to $E l = 15 \text{ kV}$, justifies the assumption

done above

so

$$\tau_2 = 15 \text{ psec.}$$

The instrumental resolution τ_{inst} is then

$$\tau_{\text{inst}} = \left[\tau_1^2 + \tau_2^2 \right]^{1/2}$$

The recording device is an optical multichannel analyser (OMA) which is coupled to the streak camera phosphor by a lens. The input stage of the OMA is an electrostatic image intensifier having a S-20 photocathode. The photoelectrons are directly focused onto an Si detector, having 500 elements, each of which being effectively 0.0025 cm x 0.5 cm in size and spaced by 25 μm from each other. This means that the OMA resolves 10 lp/mm on the phosphor of the streak camera. The readout from the Si detector array is digitized and stored in a 1000 word memory. The dynamical range of the system can be tentatively evaluated. For the streak camera, the lower current density limit is theoretically set by the minimum recordable level of light from the back phosphor, and is given by

$$\frac{dI}{ds} = \frac{\alpha \beta^2 e}{\gamma \tau K W_{0s}} \quad (\text{MKS})$$

- α sensitivity of the film or recording device
- β magnification factor of the entire system
- e electron charge
- γ phosphor conversion factor
- τ temporal resolution
- K overall light gain from the deflection stage to the film

W_{0s} mean photon energy emitted by the phosphor

With $\beta = 0.4$, $\gamma = 400$ (P. 11 phosphor), $K = 0.01$,

$\tau = 40$ psec and $\alpha = 30$ photons/30 msec - 1.25×10^{-3} cm²

(Electronical noise level of an OMA single detector element accumulated over one read-out sweep) then the minimum current density must be

$$J_{\min} = 0.85 \times 10^{-4} \text{ A/cm}^2$$

The dynamical range of the camera is then 31 db. However the Si detector array tends to saturate at a light level much lower than that allowed by the image converter tube.

2.6 EXPERIMENTAL RESULTS WITH 4 ns/cm STREAK VELOCITY

Three sets of measurements were taken with this experimental arrangement (Reference).

i) The dynamical time resolution of the streak camera/OMA system was found to be 200 psec after observation of 10 psec pulses from a Nd:Glass laser.

ii) The system was used to verify the smoothness of the micro-second long Nd:Yag pulses used for frequency up-conversion. Modulation is less than 25% of peak intensity and there is no subnanosecond fluctuations.

iii) The up-converted CO₂ pulses appeared to be shorter than the resolution limit of the system.

CHAPTER III

LOW LIGHT LEVEL, FAST SWEEP MEASUREMENTS

3.1 MEASUREMENTS WITH 1 NS/CM STREAK VELOCITY

A 5 nsec ramp generator was built and connected to the deflection plates of the image converter tube. Tests were carried out using the Nd:Yag laser in a mode-locked configuration. A 250 psec optical delay provided mean for calibration. Pulses 50 psec long could be observed. However, the dynamic range was substantially reduced due to the higher minimum light intensity required at the photocathode.

The intensity limited Nd:Yag (in Q-switch configuration) output was verified. The results previously obtained were confirmed: less than 25% intensity modulation having a period of at least 2 nsec.

CO₂ pulses less than 100 psec were observed at a signal-to-noise ratio of 2. Better and more reproducible results could be expected by increasing the sensitivity of the system.

3.2 LOW LIGHT LEVEL DETECTION

The detection assembly was modified by the insertion of a magnetically focused image intensifier between the streak camera and the OMA lead. Figure 5 shows the new arrangement. The image intensifier resolution is approximately 4 lp/mm. By magnifying in a ratio of 1.6:1 the image from the phosphor of the streak camera the effective resolution was brought up to 6.4 lp/mm which corresponds to 15 psec temporal resolution with 1 ns/cm streak velocity.

The dynamic temporal resolution was verified with the mode-locked Nd:Yag laser and pulses 40 psec long were observed. Additional measurements were carried out with no deflection voltage applied, the photoelectrons being simply focused onto the phosphor. An equivalent temporal resolution of 35 psec was found. It can be concluded that 40 psec pulses can be resolved by the system. The image intensifier was operated to give 1000:1 intensification. However the additional coupling lens collects only 1.5% of the light from the streak camera phosphor. In the worst case the signal-to-noise ratio should have increased by a factor of 10.

Figure 6 shows the display of the recorded streak for an intensity limited Nd:Yag pulse. A short period structure is present and is likely to be seen on the up-converted pulses since the 1.06 μm light acts as the "signal" in the up-conversion process.

At this stage the optical resonator of the CO_2 laser was slightly modified by using a 1.5 mm thick p-type Ge etalon instead of a 2 mm thick etalon. As indicated in Table II, the bandwidth of the new etalon is 16.5 GHz . Figure 7 shows a typical display of a 100 psec CO_2 pulse. The twin, due to a 300 psec optical delay, allows a precise calibration. Pulses as short as 80 psec are observed.

CONCLUSION

A confirmation of these results came from the observation of the output from the CO_2 laser operated in a gain switched mode and with a flat 36% reflector instead of the stalon. Some 40 psec spikes were observed which verifies that the time resolution of the detection system is still better than 40 psec. It also shows that generation of 50 psec pulses is possible.

BIBLIOGRAPHY

1. Alcock, A.J., Leopold, K., Richardson, M.C., Appl. Phys. Lett., 23, 562 (1973)
2. Alcock, A.J., Walker, A.C., Appl. Phys. Lett., 24, 299 (1974)
3. Alcock, A.J., Walker, A.C., Internal Publication.
4. Armstrong, J.A., et al., Phys. Rev. 127, 1918 (1962)
5. Bradley, D.J., et al., Optic. Comm., 2, 391 (1971)
6. Clobes, A.R., Brienza, M.J., Appl. Phys. Lett., 14, 287 (1969)
7. Grasyuk, A.Z., et al., ZhETF Pis. Red., 17, No.10, 584 (1973)
8. Lisitsyn, L.M., ZhETF Pis. Red., 9, No.5, 282 (1969)
9. Midwinter, J.E., Warner, J., Brit. J. Appl. Phys., 16, 1135 (1969)
10. Schelev, M.Y., et al., Appl. Phys. Lett., 18, 354 (1971)
11. Schelev, M.Y., et al., Rev. Sci. Instr., 43, 1819 (1972)
12. Schwartz, J., et al., Appl. Phys. Lett., 11, 242 (1967)

TABLE I

CHARACTERISTICS OF THE HIGH PRESSURE CO₂ LASER

MAXIMUM PRESSURE		15 Atm
GAS MIXTURE	CO ₂	10%
	N ₂	10%
	He	80%
DIMENSION OF THE DISCHARGE CAVITY		0.7cm×0.7cm×26cm
OPTIMUM PUMP ENERGY		300 J/l-atm
GAIN/CM AT 10.4 μm, R16 LINE, 200 J/l-atm		
	AT 12 Atm	3.5%
	AT 15 Atm	5%
OPTICAL RESONATOR		
LENGTH		1.5 m
REFLECTORS		10 m RADIUS GOLD MIRROR 1.5 OR 2 mm THICK p-TYPE Ge ETALON

TABLE II

CHARACTERISTICS OF p-TYPE Ge ETALONS

THICKNESS	2 mm	1.5 mm
RESISTIVITY	0.5 -cm	0.5 -cm
SMALL SIGNAL		
TRANSMISSIVITY	7%	10%
REFLECTIVITY	45%	50%
LARGE SIGNAL		
TRANSMISSIVITY	22%	22%
REFLECTIVITY	78%	78%
REFLECTION BANDWIDTH	12.3 GHz	16.5 GHz

TABLE III

CHARACTERISTICS OF THE IMAGE CONVERTER TUBE

ACCELERATING VOLTAGE	15 KV
ACCELERATING LENGTH	15 CM
DEFLECTING VOLTAGE	1 KV
PHOTOCATHODE	S-1
PHOSPHOR	P-11
STREAK VELOCITY	
COMMERCIAL STREAK UNIT	4 nsec/cm
MODIFIED UNIT	1 nsec/cm
RESOLUTION	
NO DEFLECTING VOLTAGE	16 lp/mm
1 nsec/cm STREAK	2 lp/mm
DYNAMIC RANGE	100:1

(Controlled by the Detecting
Device)

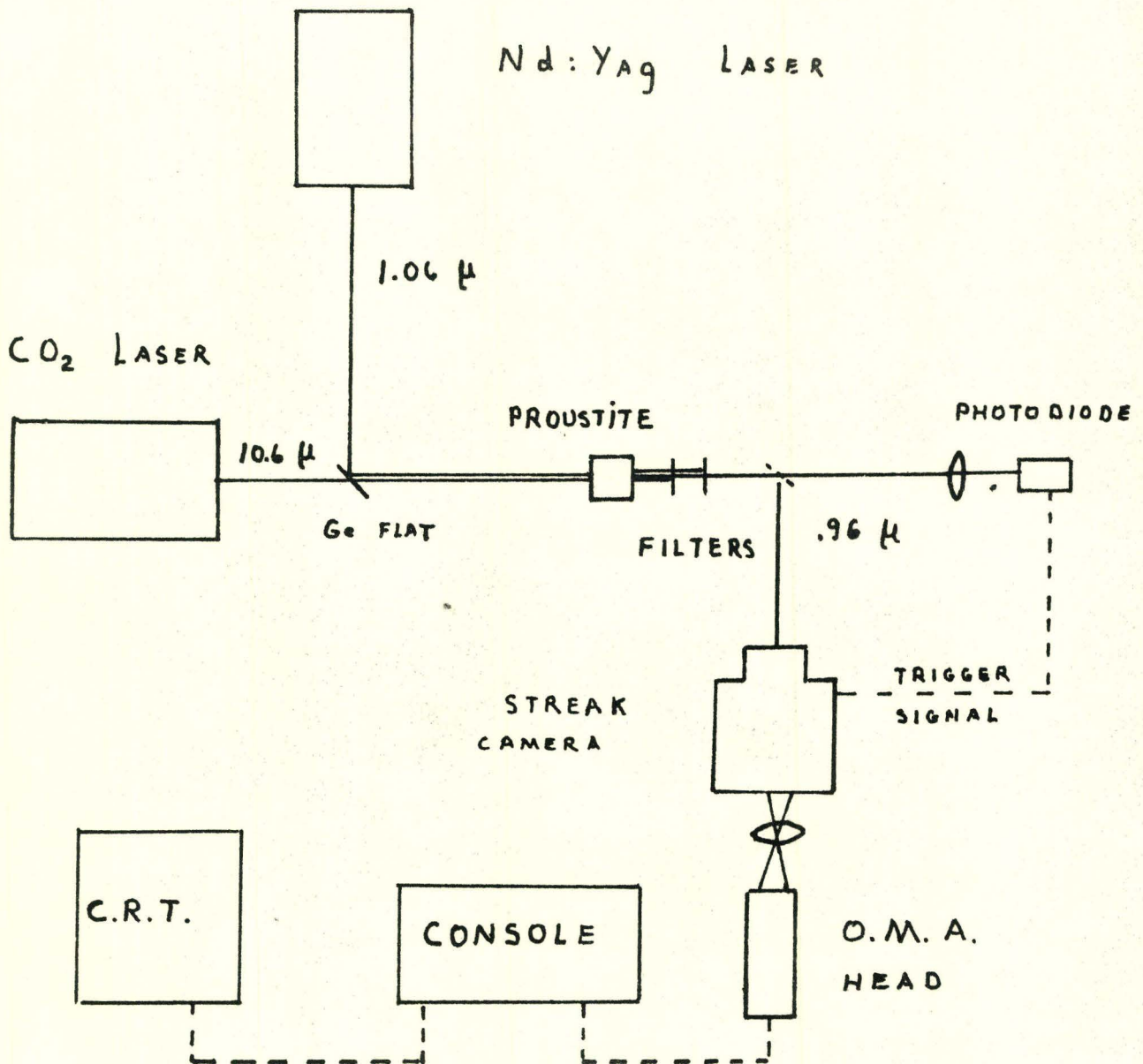


FIG 1 : Schematic diagram of experimental arrangement

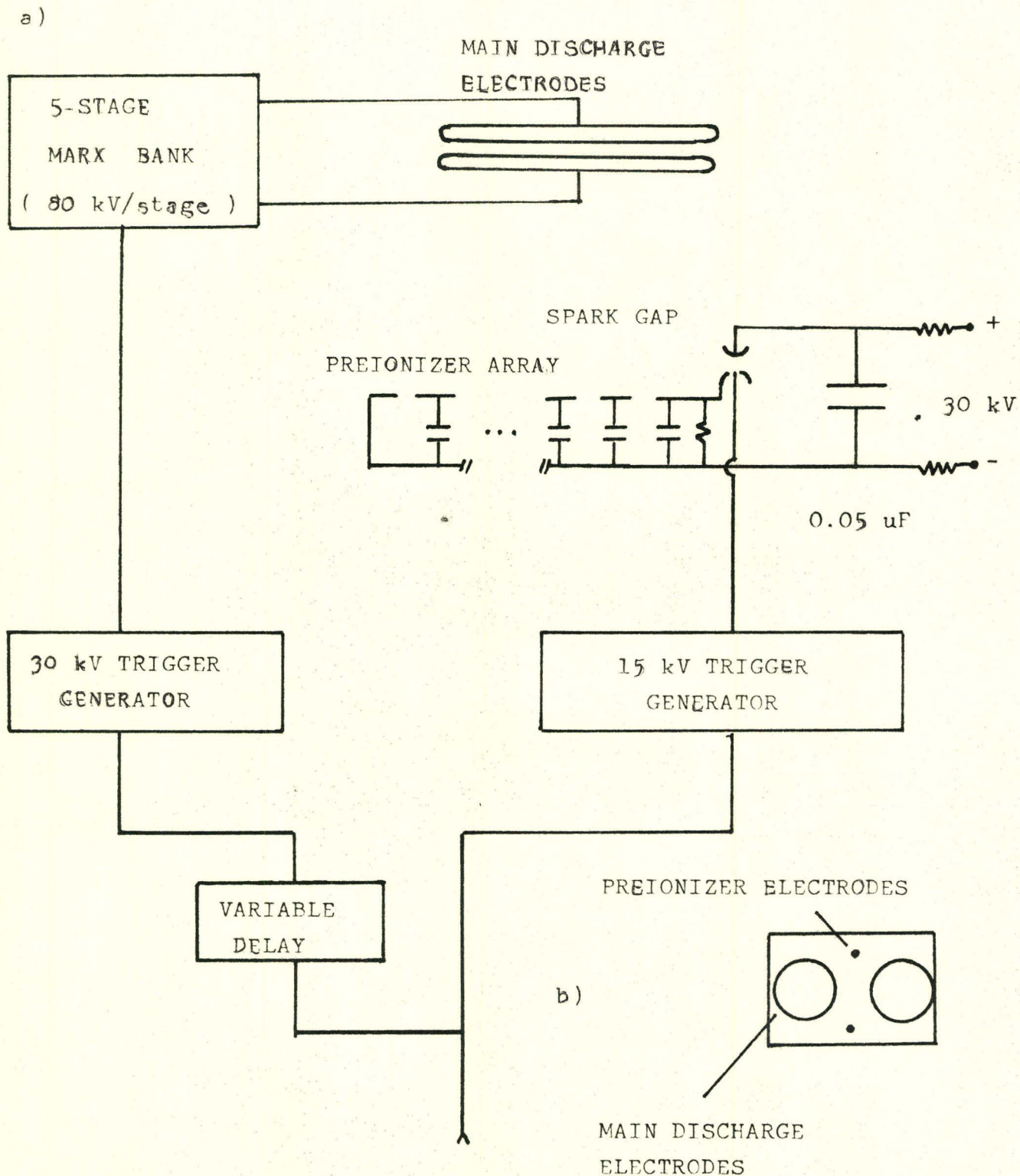


FIG 2 : a) DIAGRAM OF PREIONIZER AND MAIN DISCHARGE
CIRCUITS

b) CROSS SECTION OF LASER DISCHARGE CHAMBER

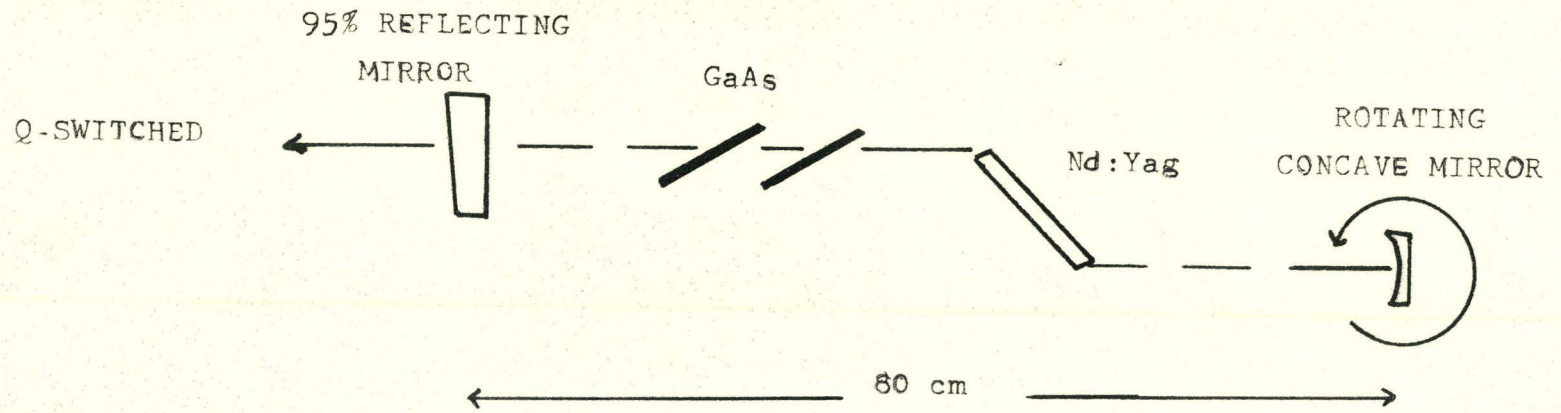
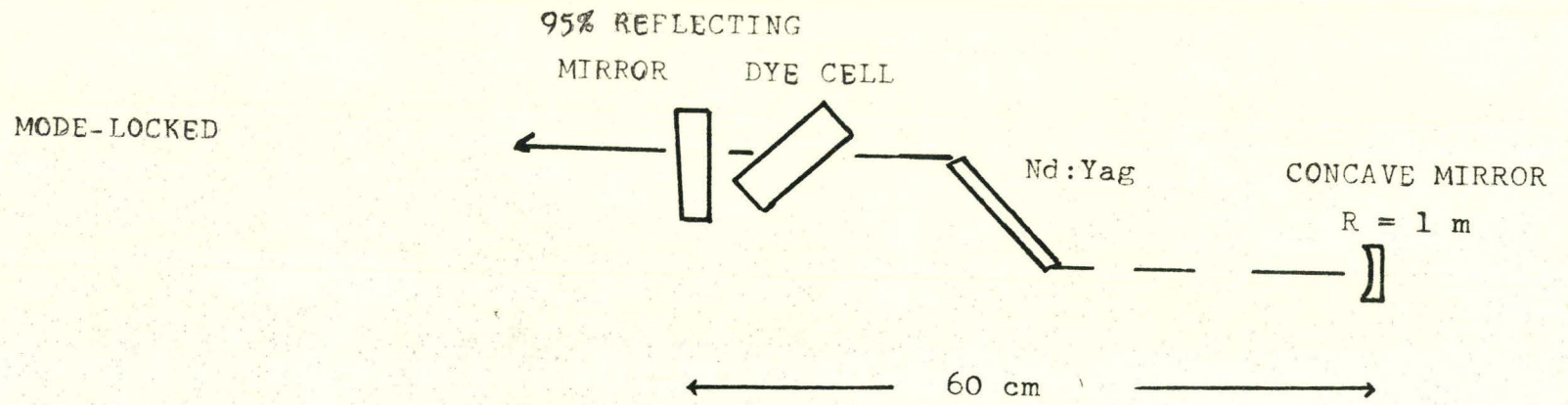


FIG 3 : MODE-LOCKED AND Q-SWITCHED Nd:Yag LASERS

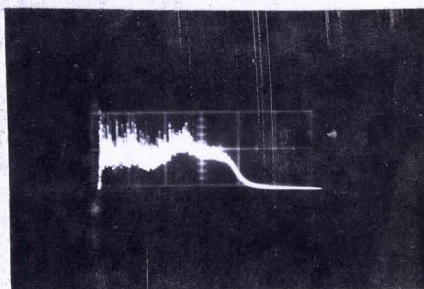


FIG 4 : RECORDING OF AN INTENSITY LIMITED
Nd:Yag PULSE (SCALE: 200 nsec/div.)

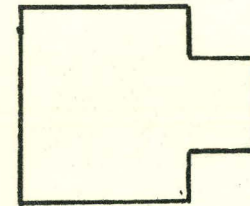
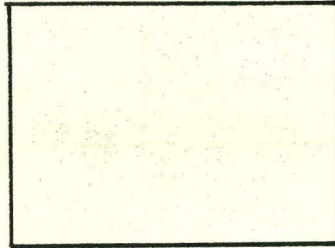
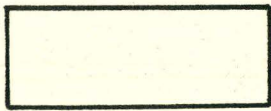
O M A HEAD

MAGNETICALLY FOCUSED
IMAGE INTENSIFIER

IMAGE CONVERTER
TUBE

$f = 8\text{cm}$

$f = 8\text{cm}$



SIGNAL
IN
←

LINEAR CONVERSION

RATIO : 0.5:1

0.74:1

1.6:1

0.8:1

FIG 5 : EXPERIMENTAL ARRANGEMENT FOR THE DETECTION OF UP-CONVERTED
CO₂ LASER PULSES

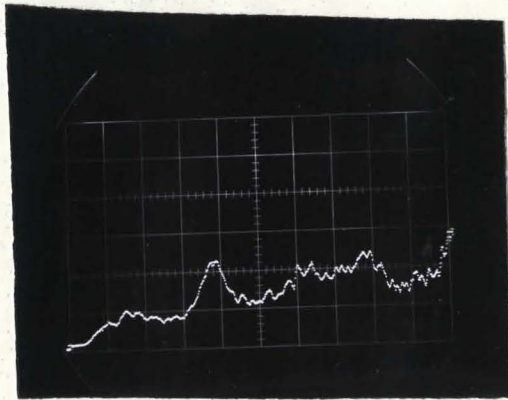


FIG 6 : DISPLAY OF AN INTENSITY LIMITED
Nd:Yag PULSE (SCALE: 200 nsec/div.)

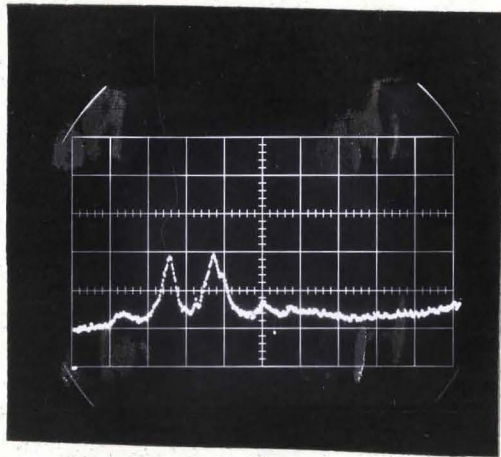


FIG 7 : DISPLAY OF A CO₂ PULSE
(SCALE: 200 nsec/div)

A THIN FILM EVAPORATOR FOR BACKSCATTERING
STUDIES

by

D.F. ROLLIN

PART B: McMASTER (ON-CAMPUS) PROJECT*

A project report submitted in partial fulfilment of the
requirements for the degree
of Master of Engineering

Department of Engineering Physics

McMaster University

September 1974

*One of two project reports: The other part is designated PART A:
INDUSTRIAL PROJECT REPORT.

MASTER OF ENGINEERING (1974)
(Engineering Physics)

McMASTER UNIVERSITY
Hamilton, Ontario

TITLE: A Thin Film Evaporator for Backscattering Studies

AUTHOR: Daniel Fernand Rollin, B.Sc. (University of Ottawa)

SUPERVISOR: Dr. J.E. Robinson

NUMBER OF PAGES: ix, 73

Dédié à Lise.

ABSTRACT

A thin film evaporator capable of producing high purity thin films (Nb, V) for backscattering studies has been constructed and tested. Evaporation is accomplished using a 3 KW electron beam at a background pressure of approximately 10^{-9} Torr. Vanadium films were characterized using several standard methods. The films were found to be continuous and relatively flat. The microscopic structure could be consistently reproduced despite large variations in deposition parameters.

ACKNOWLEDGEMENTS

The author wishes to express his gratitude to his research supervisor, Dr. J.E. Robinson for his guidance throughout the course of this work. Thanks are due to Dr. J.P. Marton for performing the ellipsometric measurements and Mike Marchand for the characteristic X-ray tests. The author also thanks Amey Singh, Fred Smith, and Lawrence Goodridge for their technical support. Mrs. Pat Skinner and Lillian Mogensen are also thanked for typing the manuscript.

The National Research Council of Canada is acknowledged for its financial assistance in the form of a Science Scholarship.

TABLE OF CONTENTS

	PAGE
ABSTRACT	iv
ACKNOWLEDGEMENTS	v
LIST OF FIGURES	vii
LIST OF TABLES	ix
INTRODUCTION	1
CHAPTER II	SYSTEM DESIGN
2.1	Design 2
2.2	Pumping Capacity and Operation 2
2.3	The Active Region 3
CHAPTER III	SUBSTRATE PREPARATION
3.1	Selection of the Substrate 6
3.2	Substrate Preparation 6
CHAPTER IV	THIN FILM THEORY
4.1	Introduction 11
4.2	Nucleation and Growth 11
4.3	Structure 12
CHAPTER V	CHARACTERIZATION OF THIN VANADIUM FILMS
5.1	Introduction 19
5.2	Electron Microscopy 20
5.3	Optical Microscopy 25
5.4	Electron Microprobe 27
5.5	Characteristic X-rays 28
5.6	Resistivity 29
5.7	Ellipsometry 30
CONCLUSION	32
BIBLIOGRAPHY	33

LIST OF FIGURES

FIGURE		PAGE
1	SCHEMATIC DIAGRAM OF THE COMPLETE SYSTEM	35
2.	3-D VIEW OF EVAPORATOR AND TARGET CHAMBERS	36
3	PHOTOGRAPH OF THE SYSTEM	37
4	EXTERNAL ASPECT OF EVAPORATOR-TARGET ARRANGEMENT	38
5	INTERNAL ASPECT OF THE SYSTEM	39
6	EVAPORATION CHAMBER	40
7	METAL VAPOUR SHIELD	41
8	DEPOSITION RATE vs VAPOUR PRESSURE	42
9	EXTERNAL CONTACT ANGLE OF WATER DROP ON GLASS	43
10	APPARATUS FOR CLEANING SLIDES IN ALCOHOL VAPOUR	44
11	NUMBER DENSITY OF GRAINS vs THICKNESS	45
12	(a) and (b) EFFECTS OF VARIOUS PARAMETERS ON GRAIN SIZE	46
	(c) EFFECTS OF VARIOUS PARAMETERS ON GRAIN SIZE	47
13	DENSITY OF VANADIUM FILM vs THICKNESS	48
14	CRITICAL THICKNESS vd DEPOSITION RATE	49
15	(a) and (b) EFFECT OF INCREASING THICKNESS ON RESISTIVITY	50
	(c) and (d) EFFECT OF INCREASING THICKNESS ON RESISTIVITY	51
16	PARAMETERS OF SAMPLES	52
17	STEREO ELECTRON-MICROGRAPH OF FILM SURFACE	53
18	ELECTRON-MICROGRAPHS AND CORRESPONDING DIFFRACTOGRAPHS	54
19	PLOT FROM ELECTRON DIFFRACTION	61

20	ELECTRON MICROPROBE	62
21	MASS ABSORPTION COEFFICIENT OF VANADIUM	63
22	CONTINUOUS PLOT OF INTENSITY OF X-RAYS ALONG THE FILM	64
23	INTENSITY DISTRIBUTION OF X-RAYS	65
24	V-I PLOT FOR RESISTIVITY	66
25	RESULTS FROM RESISTIVITY MEASUREMENTS	67

LIST OF TABLES

TABLE		PAGE
I	EFFICIENCY OF ULTRASONIC CLEANING	68
II	EFFICIENCY OF VARIOUS CLEANING PROCEDURES	69
III	DESCRIPTION OF TWO SERIES OF MICROGRAPHS	70
IV	ALLOWED (hk1) VALUES FOR DIAMOND FCC AND BCC STRUCTURES	71
V	CHARACTERISTIC X-RAYS	72
VI	ELLIPSOMETRIC MEASUREMENTS	73

CHAPTER I

INTRODUCTION

The construction of the thin film evaporator described in this report is part of a larger system constructed to study the interaction of fast particles with solids. The experiment employs backscattering techniques using keV energy protons incident on thin films (100 Å to 1 μm) of Vanadium or Niobium. The experimental system consists of a proton source, an evaporator, a target chamber, and a scattered particle detection device (see Fig. 1).

Extremely pure samples are needed for the target. In order to have clean and oxide free samples, it is necessary to prepare the targets in situ under ultra high vacuum conditions. The desired characteristics of the evaporator are:

- (i) operation at high vacuum,
- (ii) the capability of producing high quality films, and
- (iii) reproducibility of the films.

The design of the evaporator is presented in Chapter II. Chapter III contains a brief review of the thin film theory and the results from the characterization of the films are given in Chapter IV.

CHAPTER II

SYSTEM DESIGN

2.1 Design

In order to meet the spatial specifications, a planar configuration has been adopted. The general lay-out of the system is shown in Fig. 2. A photograph is given in Fig. 3. It consists of stainless steel evaporation and target chambers interconnected by a 4-1/2" flange. The interconnection also acts as an aperture for the vapour beam. The pumping units are a 50 l/s and a 100 l/s ion pumps and a titanium sublimation pump. A planar T-shape design was adopted to differentially pump the target chamber during evaporation. This configuration provides economy of space along the evaporation axis (vertical) and the ion source axis (horizontal).

2.2 Pumping Capacity and Operation

To start the system, an oil free sorption pump is used. The pressure can be brought down to 2-5 microns with this pumping stage. The roughing pump is then isolated from the system by a metal valve which is also used as air inlet when venting the system. At a pressure less than 5 microns, all high vacuum pumps can be started. The ion pumps can reduce the pressure to 2×10^{-9} Torr. Sublimation pumping reduces this another order of magnitude.

The sublimation pump acts as a booster at high vacuum. For the ideal case, the pumping speed of a surface covered with titanium

can be calculated from:

$$S_p = \frac{A \cdot S_i \cdot C_{ap}}{A \cdot S_i + C_{ap}} \quad (1)$$

where A is the area of a specific deposition surface, S_i is the specific pumping speed per square inch of titanium deposition surface. For pure N_2 and a surface temperature of $20^\circ C$, S_i is 30 l/sec - sq. in. At $-195^\circ C$, S_i is 65 l/sec - sq. in. C_{ap} is the conductance of a circular inlet with aperture diameter D. This is defined as

$$C_{ap} = 75 \frac{\pi D^2}{4} \sqrt{\frac{T}{298}} \quad (2)$$

where T is the absolute temperature of the gas. It has been noticed that some titanium deposition occurred on part of the target chamber. Adding contribution from various surfaces, a N_2 pumping speed is calculated to be

$$(S_p)_{tot} = 2210 \text{ l/sec}$$

2.3 The Active Region

The main parts of the system are the evaporation and the target chambers. Referring to Fig. 4, a list of the uses of the parts which are all 1-1/2" internal diameter flanges is presented below:

Evaporation Chamber:

A': Cooling line for the electron gun evaporator.

B', C': Electrical feed throughs for the electron gun.

D': Window.

E': Blank. Will eventually receive a mechanical feed-through that will activate a shutter.

Target Chamber:

A'': Temporary fixed sample holder. Projected sample holder will be rotatable about the x-axis.

B'', C'': Blank. Will eventually be connected to the detection system and to an ion gauge.

D'': Blank. Will be the entry port from the proton source.

E'': Cooling line and electrical feed-through for the thickness monitor sensor head.

F'': Blank.

G'': Valve and roughing pump.

Figure 5 shows the lay-out of the instruments inside the system. Internal structures of pumps are not shown.

Figure 6 is a close-up of the evaporator surrounded by its metal vapour shield (with one side removed). The filament F, acting as the cathode, is at a voltage of - 4000 volts. The potential drop across it is 0 to 6 volts for a current of 0 to 25 amperes. This produces an emission current of 0 to .75 amperes; 99% of emitted electrons hit the material pellet.

The use of the shield (detailed in Fig. 7) is to prevent breaking down between the high voltage leads L_1 or L_2 and any other part of the chamber. The causes of breakdown are:

- (i) high pressure (10^{-6} Torr) evaporant gas,

- (ii) drops of melted vapor expelled from the pellet, and
- (iii) small flakes of material released from the walls of the evaporation chamber.

For these last two causes, additional protective "flaps" have been added.

The thickness of the film is measured using a quartz crystal oscillator. The assembly consists of the internal oscillator head and a digital monitoring unit which is completely automatic. Thickness is computed directly from the frequency shift of the oscillator and the density input, and is given to a digital accuracy of 1, 10 or 100 Å according to the scale used. This amount is an average over the crystal area (1 cm^2) and contains an error due to the microscopic structure of the film. Hence the term "quartz oscillator thickness" is used.

CHAPTER III
SUBSTRATE PREPARATION

3.1 Selection of the Substrate

The central requirement of the substrate is that it does not introduce effects which could prevent the formation of thin, high purity, uniform films.

The desired substrate properties are:

- (i) a flat surface,
- (ii) no strong structural features to prevent formation of epitaxial growth, and
- (iii) easy handling with regard to examination of films with an electron microscope on other standard diagnostic techniques.

The selected material was soda-lime glass in the form of commercially available imicroscope slides (75 mm x 25 mm x 1 mm). The chemical composition is:

72.68%	SiO ₂
12.95%	CaO
13.17%	NaO

3.2 Substrate Preparation

The slides did not require extra polishing due to the high quality of their surfaces finish. However, extremely good cleaning was needed. The two contaminants which must be eliminated are large dust particles and a layer of organic compounds such as oil, greases,

etc. This second one is by far the more important since this layer of grease, no matter how thin it may be, ruins the quality of the surface.

The efficiency of a cleaning method can be estimated by various means as listed below.

(i) The coefficient of friction (u_s or u_k) increases with the degree of cleanliness. This is estimated using a standard glass surface or a piece of cloth.

(ii) When a drop of water is put on a surface, the surface tension can be overcome by hydrogen bonds between the water molecules and the ions embedded in the glass surface. As a result, the drop internal contact angle is very small (see Fig. 9).

(iii) Breath figures are a consequence of the previous method, on a macroscopic scale. When the contact angle is high, water vapour is deposited on a cold surface as droplets so that a breath figure is visible. When the contact angle is low, water forms a uniform, invisible layer. Methods for cleaning glass that were available here can be subdivided into three classes.

(a) Flame cleaning The surface is exposed to a very hot flame. This forms a fresh surface by melting a thin layer of glass on the side opposite to the one exposed to the flame. This method did not give satisfactory results in the present experiment due to the very low thickness of the slides.

(b) Ultrasonic agitation This method is good for removing large particles. The slides being cleaned are kept in a bath of organic solvent while agitated so that chemical action is present as well. Table I gives

"Lissapol N" : nonionic, polyethylene glycol active agent

Boiling solutions of "Alconox", similar to Teepol, were used here.

(iii) Organic solvents. The organic solvents are the only reagents that attack contaminants such as oil or grease. They can be used in various ways such as baths, on cotton wool or in vapour degreasing apparatus. The evaporator used for the present experiments is shown in Fig. 10. It uses ethyl alcohol which condenses on the slides, dissolves the contaminants and drips back into the bath. The cooling coil prevents excessive loss. The slides could be kept five minutes in the evaporator before they became too hot to condensate any solvent. This method is used as the very last step in the cleaning procedure.

Taken from Holland⁽¹²⁾ Putner⁽¹⁸⁾ and Fray,⁽⁹⁾ Table II gives efficiency of various solvents and cleaning procedures. Note that Fray estimates the cleanliness by the ease with which a titanium point scratches the surface. The weight applied on the point is given. Some other cleaning method such as vacuum melting and ion bombardment are also given but will not be discussed here.

The complete cleaning procedure used for the present experiments is as follows:

- (i) cleaning with cotton wool and acetone,
- (ii) boiling for 20 minutes in a solution of Alconox detergent,
- (iii) rinsing 20 minutes in boiling demineralized water,
- (iv) cleaning 20 minutes in gently boiling ethyl alcohol,

- (v) cleaning 10 minutes in the ultrasonic agitator (slides are in a hot alcohol bath in the agitator), and finally,
- (vi) cleaning 5 minutes in alcohol evaporator.

The slides are then allowed to cool and then put back in the evaporator.

This is done many times. Immediately after this procedure, the best slide is selected and placed under high vacuum.

CHAPTER IV

THIN FILM THEORY

4.1 Introduction

The processes by which a film comes into being have been described in many books and review articles. (See reference 8, 11, 16, 17). The theoretical models are fully developed in the above references. A good bibliography for the subject can be found in both Chopra⁽⁸⁾ and Holland⁽¹¹⁾ especially concerning original papers.

Many successive processes are responsible for the formation of a film. But in all of these, a thermodynamical equilibrium is involved between the vapour phase and a "film phase". The latter is really a two-dimensional vapour phase on the surface of the film.

4.2 Nucleation and Growth

Consider an individual atom hitting the surface of the substrate (which can be visualized as a lattice of spring connected masses). The atom loses its velocity component normal to the surface and becomes an "adatom" loosely bound to the surface by bipolar and quadripolar forces. "Nuclei" form when atoms collide and stay bounded into clusters. These clusters grow in size.

For simplicity, it can be assumed that each individual nucleation center grows into a single crystal.

The next step is the growth of these nucleation centers, at this stage called "islands". Initially the process is a simple continuation

of the initiating growth of the centers. But a stage is soon reached by large islands where they pick up atoms from three sources:

- (i) adatoms impinged on surface of substrate between islands,
- (ii) coalescence with smaller islands (it has been noticed (reference 3) that small islands migrate), and
- (iii) vapour-solid phase transition on the surface of the islands.

This continues until the large islands scinter together to form a continuous film. The thickness at which this event occurs is called the critical thickness. Subsequently, the film grows by vapour-solid phase transition only.

For a very good illustration of the complete sequence of processes involved, see references 4, 8, 11.

4.3 Structure

The interesting aspects of the structure of films are

- (a) the grain size,
- (b) the surface roughness,
- (c) the density and other bulk parameters, and
- (d) the lattice constant and atomic structure.

(a) The grain size The assumption done earlier stating that each individual nucleation center is a monocrystal can be extended. Since the small islands seem to show a certain mobility, the resulting island after sintering of two (a small and a large island) could be monocrystalline. Thus during coalescence, the smaller nucleus could be rotated to suitably

fit the lattice structure of the larger. The subject is still very much debated. However, Fig. 11 shows a compilation done from a series of micrographs, by Basset et al.,⁽⁴⁾ of a gold on rocksalt film. Migration of small islands is conclusive from the drastic drop in number and the non linear increase in size at thickness where the film is not continuous.

Some very qualitative graphics were given by Chopra for metals (see Fig. 12). If one follows his descriptions through his voluminous work, it can be understood that low T_s (temperature of substrate) means 80°K and high T_s is the melting point of material under study. Low deposition rate is 1 Å/sec while the opposite is 20 Å/sec. Thickness usually ranges from 50 Å to 5000 Å in the experiments done by him or cited. Grain size is usually within 40 to 4000 Å.

(b) Surface Roughness At low temperature the surface mobility of adatoms is small and hence we approach the conditions of a perfect random deposition. The standard deviation from the average film thickness is then:

$$\Delta t = \sqrt{t} \quad (3)$$

The use of a non-crystalline substrate enhances the random deposition process by restricting the occurrence of epitaxial growth.

From the random deposition case smoother films can be obtained according to specific conditions. These are a high substrate temperature (reference 1) as mentioned, a low deposition rate and a high vapour temperature (reference 15). Magnitudes of temperatures are determined with respect to the melting point of the metal (Vanadium - 1890°C). All these conditions create a thermodynamical system with a long relaxation time so

that adatoms can distribute evenly over the surface. For the actual experiment, the substrate was at room temperature (low) but the evaporation temperature was in excess of 3500°C. The deposition rate was varied but ranged up to approximately 10 Å/sec (which is low).

(c) Density and other bulk parameters Density is a crude gauge for many microscopic properties of the film. These properties are:

(i) Lattice constant. This will be discussed in more detail in section d.

(ii) Porosity. This is related to the extent to which the film becomes continuous after the islands interconnect. Thickness dependence of density is shown in Fig. 13. The reader may also refer to micrographs in a book by Holland (11 - Plate 11). Pictures in succession for a fast and a slowly deposited Ag on glass films show the existence of "channels" (holes in between interconnected islands) long after reaching the critical thickness t_c . It should be noticed that t_c is smaller for the higher deposition rates. Table IV gives a description of these micrographs. Chopra and Randlett⁽⁷⁾ gave opposite results, at least for low deposition rates (see Fig. 14).

Resistivity monitoring experiments have been performed by many researchers. In these experiments, the resistivity was continuously measured while depositing a metal film. Typical results from Chopra^(5,6,7) are given in Fig. 15. When the thickness of the film reaches the critical point, the resistivity drops by several orders of magnitude. Thereafter, the continuous film has a resistivity which is well above the value for bulk material. This is due to:

First, the low thickness which is less than the mean free path of electrons. We can express the resistivity as

$$\rho_{\text{film}} = \frac{mv}{ne^2 l_{\text{eff}}} \quad (4)$$

with

$$l_{\text{eff}} = \frac{l}{1 + 3/8\gamma(1-p)} \quad (\gamma \gg 1) \quad (5)$$

or

$$l_{\text{eff}} = 3/4 \frac{1+p}{1-p} t \ln(1/\gamma) (\gamma \ll 1) \quad (6)$$

where

- ρ_F : resistivity
- n : density of free electrons
- e : electronic charge
- m : electronic mass
- v : average velocity of electrons on the Fermi surface
- l_{eff} : effective mean free path
- $\gamma = t/l$: thickness of film over bulk material mean free path
- p : probability of electron elastic scattering of the surfaces of the film

Full development of the theory can be found in reference 2, 16.

Secondly, the porosity of the film will increase the resistivity by the obvious increase in boundary terminations of electron free flight. In addition, porous films will conduct electric current through various tunnelling processes and will exhibit a characteristic non-ohmic behaviour.

Some of these processes and their predicted high electric field e

(in the order of 10^3 V/cm) dependancies are:

- thermionic or Schottky emission

$$1/p \propto \exp\left[e^{3/2} \frac{\sqrt{\epsilon}}{kT}\right] \quad (7)$$

k: Boltzman constant

T: absolute temperature

- quantum mechanical tunneling

$$1/p \propto \exp\left[\frac{\text{constant}}{\epsilon}\right] \quad (8)$$

- activated tunneling

$$1/p \propto \exp\left[\frac{1}{kT} \left(\frac{2e^{3/2} \sqrt{\epsilon}}{\epsilon} + re\epsilon\right)\right] \quad (9)$$

ϵ : dielectric constant

r : average size of islands

In all cases low field behaviour is ohmic.

(d) The lattice constant and structure Vanadium has a bcc structure and has a lattice constant $a_0 = 3.028$ A. Departures from this value are not expected as minute variations in lattice parameter have been observed only in very thin films (where the ratio area over volume is large) and for specific lattice directions.

However, large scale variations could be found due to the causes listed below.

(i) Large impurity contents could exist on the film. Most likely these impurities could be gases remaining in the system or metal vapours such as Ti (from the sublimation pump) or Fe, Ni, etc., accidentally

evaporated from the electron-gun casing. It is known that gases in concentration exceeding one percent will produce amorphous films. The effect of metals is much more complex since alloys are formed. However, metals with different lattice systems will produce amorphous structure.

(ii) Deposition parameters such as substrate temperature and deposition rate could have an effect. In the actual experiments, the glass slides were kept at room temperature. So no effect could be expected since temperature needs to be less than 80°K to produce amorphous film (see reference 8). Deposition rate was the only variable parameter. For vanadium high deposition rates may produce fcc structure and ultimately amorphous structure (see reference 7).

(iii) Formation of oxides could be preset on the surfaces. It was expected that an oxide layer would grow on the surface of the air exposed films and eventually interfere with the electron diffraction tests carried on the films. However, means of detecting and getting rid of this effect will be presented in the next chapter. The most serious difficulty from the oxide layer formation was that the vanadium film could be completely oxidized after a certain length of time. This cannot occur if the ratio of the molar volume of oxide to the molar volume of the metal is more than one i.e., the oxide layers entirely recover the metal film and after reaching a certain thickness, shields the metal from further oxidization. For the various vanadium oxides the ratios are:

$$V_2O_2 \quad 1.51$$

$$V_2O_3 \quad 1.82$$

$$V O_2 \quad 2.12$$

It is of interest to notice that the processes of formation of an oxide film are the same as those previously explained for a metal film except that the oxygen becomes chemically bound to the metal (see reference 19).

CHAPTER V

CHARACTERIZATION OF THIN VANADIUM FILMS

5.1 Introduction

Following from the topics presented in the preceding chapter, several methods of characterization were used on samples with a wide range of deposition parameters. Some aspects of the deposition process were standardized such as

- (i) the geometry of the evaporator,
- (ii) the "backing vacuum" (i.e., the pressure at which evaporation was initiated) was always between 4 and 8×10^{-8} Torr, with pure N_2 gas filling the system before pumping down,
- (iii) the nature and cleaning process of the substrate, and
- (iv) the substrate was kept at room temperature at all times and the films were not annealed. Actually, only two conditions could be varied: the thickness and the deposition rate. Figure 16 shows the values of these parameters for all the films deposited for this work. The dashed line indicates the low thickness high rate limit of the evaporator. It can be noted that, according to the results from various workers (see Chapter III), the range of the deposition rate is too small to allow observation of variations in the properties of the films.

The techniques used for probing the films were:

- (i) optical and electron microscopy,
- (ii) electron diffraction,
- (iii) electron microprobe,

- (iv) characteristic X-rays,
- (v) electrical resistivity measurements, and
- (vi) ellipsometry.

5.2 Electron Microscopy

(a) Introduction

Most of the characterization work has been done with electron microscopes. The specific purposes were:

- (i) to determine the quality of the glass surface on the point of view of roughness,
- (ii) to estimate the uniformity of the films and correlate with observations under the optical microscope,
- (iii) to determine the grain size, and
- (iv) to explore the lattice structure.

For the last two points, correlations with evaporating conditions were closely examined.

(b) Scanning electron microscope

With this technique samples are usually coated with a thin gold reflecting film to reveal the structures of the surfaces. This technique is ideal to study glass surfaces covered with vanadium films. In order to prevent re-evaporation by the e^- -beam, the magnification was limited to 3000 X. At this magnification, the surface structure of the film cannot be seen. However, electrons accumulate on non conducting surfaces revealing as white spots the discontinuities and the pores in the film. Figure 17 shows a stereo view of the surface at 2000 X magnification of

a typical thin film. Dust and holes in the film are identified as well as a pit in the glass (upper right). Magnifications up to 2500 X with a resolution of less than 0.5 μm indicated a very smooth glass surface. Very few scratches were seen and they were all less than 1 μm wide. Holes in the film were more frequent. They were probably due to metal deposition on dust particles left on the glass slide after the cleaning procedure.

For economic reasons, as well as simple convenience, correlation between optical and scanning electron microscope observations were attempted. Except for an easier identification of holes in the films, the attempts were unsuccessful due to the very low depth of field of the optical microscope compared with the electron microscope.

(c) Transmission electron micrographs

The next two topics concern the use of the transmission electron microscope to obtain micrographs and diffractographs. For those cases, the samples had to be prepared in a special way. That is, the films had to be peeled off of the substrate and placed on a mesh to permit the electron beam to penetrate through the sample. In order to accomplish this, a very thin layer of hard wax was melted on the glass slides. After deposition, small pieces of the film could be floated away when dipped in acetone. It was expected that this method would lead to locally good films over an area having the size of the field of view of the microscope.

Some typical micrographs are shown on Fig. 18. They should be compared to series of photographs by Basset et al., (reference 3, page 35) and Chopra (reference 8, pages 164-166) where the growth of metal films

is shown at various stages. The size of grains is less than 100 \AA . For the thinner film ($t = 335 \text{ \AA}$) it ranges from 200 to 500 \AA and for the thicker film ($t = 1592 \text{ \AA}$) from 700 to 1000 \AA . In this last case, there seems to be a second layer of crystallites, that account for the thickness. The grains are interconnected and it is possible that many neighbour grains have a common orientation of their lattice since few sharp boundaries are seen. Low magnification micrographs show the uniformity of the film. Darker areas on Plate 209 are wax spots.

(d) Transmission electron diffraction

Electron diffraction patterns of areas examined by electron microscopy are produced in Fig. 18. An estimate of the size of the grains can be done by inspection using a number of guide rules:

- (i) hazy halos as rings indicate an amorphous structure,
- (ii) clean continuous rings are typical from polycrystalline samples with a grain size of approximately 100 \AA ,
- (iii) spotty or grainy rings are due to crystallites approaching the size of the electron beam diameter, perhaps 1/100 to 1/10 of it, and
- (iv) if the pattern is a systematic array of spots, the electron beam hits only one crystal.

In the actual case, the selector aperture which determines the size of the beam was 50 \mu m in diameter. From the diffractographs it is clearly seen that case (iii) is applicable. The grain size can be estimated to range between $5,000 \text{ \AA}$ to 5 \mu m . The lattice structure can also be identified and the lattice parameter can be calculated. Consider a sample being

irradiated by a collimated electron beam. The scattered beam is collected on a photographic plate at a distance L .

The Bragg's law relation is

$$n\lambda = 2d \sin\theta$$

with

$$\lambda = \frac{h}{2mE} \quad (10)$$

and where the symbols have their usual meaning.

The spacing between plane of atoms in a particular direction $h k l$ is

$$d_{hkl} = \frac{a_0}{\sqrt{h^2 + k^2 + l^2}} \quad (11)$$

Finally the scaling of the rings due to the configuration of the camera is

$$\lambda/d_{hkl} = \frac{R_{hkl}}{L}$$

or

$$d_{hkl} = \frac{L\lambda}{R_{hkl}} \quad (12)$$

which is another form for Bragg's law.

R_{hkl} : radius of the ring produced by the set of planes $h k l$.

This subscript implicitly includes n .

L : distance from the sample to the photographic plate. L is known as the camera constant (see reference 10, page 174).

Combining equations (11) and (12)

$$R_{hkl} = \frac{L\lambda}{a_0} \sqrt{h^2 + k^2 + l^2} \quad (13)$$

The procedure is then to plot the values of the square root (from Table IV) versus the radius of the corresponding ring (see Fig. 19). The camera constant can be found using the same procedure with a sample of gold, where

$$(a_0)_{Au} = 4.0786 \text{ \AA}$$

The result was

$$(a_0)_V = 3.40 \text{ \AA}$$

(e) Reflection electron diffraction

In this case, samples with vanadium films deposited on glass could be used. The electron beam incident on the film is at a grazing angle penetrates only to a depth of a few hundred angstroms into the film. The films used were more than 1000 \AA thick to prevent reflection off of the substrate. Figure 18, plate 260, shows a typical diffractogram. The information contained in these are the same as in the case of transmission diffraction.

The effective size of the electron beam on the film is approximately 300 \mu m which explains the continuous rings. The lattice parameter was calculated: 3.65 \AA and 3.90 \AA .

A probable error of more than 10% was present in the measurement of the radii of the rings for both methods. A microdensimeter ought to be used for these measurements. However, the exact value of the lattice parameter has no significance in itself if the samples are pure (no alloy). In all cases, a bcc structure was observed.

5.3 Optical Microscopy

Initially it was thought that fresh films could be examined under the optical microscope before long exposures to air cause contamination. However, some difficulties were encountered. These are listed below:

(i) Low depth of field cause certain difficulties. Actually this could be advantageously used to explore the depth and position observable features onto or below the film. However, it was very difficult to focus precisely on the film.

(ii) Poor resolution inherent to visible light is another problem. At useful magnification for film exploration (approximately 1000 X) and for the size of the objects to be observed (1 μm for irregularities in the glass or the film) the resolution was so poor that very few features could be positively identified. On the other hand, some methods could help such as:

(i) Observations can be correlated with the scanning electron microscope. As explained earlier, this attempt was almost unsuccessful except for a better discrimination between dust particles and holes in the film. Furthermore, the fact that the glass surface was found to be extremely uniform; therefore, virtually eliminating the possible explanation

of pits in glass in the identification of doubtful features.

(ii) One can correlate observations using three types of illumination: through the film, reflection, and grazing incidence. In the first case, the metal film (which is partially transmitting due to its low thickness) produces a dark field. Holes in the film appeared white and most other features black. By reflection, the film was bright, holes in the film were black. Other features were either sparkling (dust particles loosely bound to the film) or black. The third type of illumination puts into evidence irregularities out of the plane of the film.

The microscope used was a Zeiss Teltraphot II having a resolving power of $.15 \mu\text{m}$. Among its various features, the illumination could be changed instantaneously without disturbing the sample.

The observations can be summarized. The size of the holes range from a fraction of μm up to $10 \mu\text{m}$. All were resolvable so that they were larger than approximately $.1 \mu\text{m}$. They usually tend to cluster in groups of five or less, each hole being separated by hundreds of atoms from the other. The clusters were separated by distances of a few millimeters. This pattern was the same for dust collected on the surface of the film. It is likely that the holes originated from dust particles that were not removed by the cleaning process.

Other interesting features were spots of organic material (grease, oil, etc.) left after cleaning and imprisoned under the film. These appeared when the cleaning procedure was carried out too quickly.

5.4 Electron Microprobe

This technique was used to produce a film profile. The experimental arrangement is schematically illustrated in Fig. 20. An electron beam having an energy of 40 keV is incident on the sample. It excites the lower levels of atoms. The X-radiation is then collected by a proportional counter and analysed. One K line from the silicon atoms in the substrate is then selected and its intensity is monitored as the sample is transversely scanned. The attenuation is a function of the thickness of the vanadium film, that is:

$$I_{\text{collected}} = I_0 e^{-ut^*} \quad (14)$$

where I_0 is intensity of the radiation emitted in the direction of the detector by the excited region in the substrate and u is the mass absorption coefficient. Using Fig. 21 which is plotted with data from reference 14, it is found that

$$u = 1750 \text{ cm}^2/\text{gr}$$

for vanadium at 7.11 \AA (Silicon K line). t^* is the mass equivalent thickness.

The logarithm of the number of counts is directly proportional to the thickness:

$$\ln(I/I_0) = -u\rho t \quad (15)$$

with

$$\rho t = t^*$$

Figure 22 shows a continuous plot of the intensity with a resolution of $.25 \mu\text{m}$. A digital output gave the number of counts from the proportional detector integrated over 10 seconds while the scan rate was $2.5 \mu\text{m}/\text{sec}$. Figure 23 is a bar diagram showing the distribution of the logarithm of the number of counts. It exhibits a roughly normal distribution curve with a half width equivalent to a variation of 45 \AA in thickness. The crystal quartz thickness of the sample was 1723 \AA so that the measured fluctuation in thickness corresponds to the predicted t law for cold substrate films (see Chapter IV).

5.5 Characteristic X-rays

This method was used to detect impurity metals in the films. The sample used was relatively thick (1500 \AA) such that small traces of impurities could be detected. It should be noted that this film was deposited while testing was still being undertaken of the electron-gun. It is the worst possible case.

The sample was bombarded by x-rays from a tungsten target. These x-rays excite the low level electrons to produce the characteristic spectra of the elements. Intensity measurements can give relative quantities. Since a calibrated sample was not prepared, the exact impurity content remains unknown. Table V gives the estimated results. The first column lists the possible elements. The tests were carried out on the film itself, on a bare glass slide and with no sample at all. It was found that the soda lime glass contained non negligible amounts of Fe and other impurities. A possible source of Fe, Ni and Mn in the film

was material from the electron-gun casing which could be evaporated by the misaligned beam. The small difference in counting rates (which appeared persistently in all tests) could be due to an estimated film impurity content of less than 100 ppm. More likely this difference can be accounted for by different impurity concentrations in the two glass slides. Titanium was suspected due to the use of a titanium sublimation pump. Although no further tests were tried, it is expected that later films, produced with a carefully adjusted evaporator, contain negligible amounts of impurity metal atoms.

5.6 Resistivity

Resistivity measurements were attempted on the film after long exposure to air. These measurements were very incomplete since they lack time continuity (cf. measurements done by Chopra and presented in Chapter III) and high fields necessary to detect non linear porosity effects.

The instrument used was a four-point microprobe with a low current source. The procedure used is the standard voltage (V) vs current (I) graphs for I ranging from 1 to 9 μ A. The resistivity is given by

$$\rho = 4.53 \cdot 10^{-8} \frac{\Delta V}{\Delta I} t \quad (16)$$

(see reference 21, page 42) where t is the thickness of the film in A units, Fig. 24 is a typical V-I plot showing various slopes corresponding to different positions of the probe on the film. These variations in

resistance can probably be accounted for by variations in thickness.

The non-zero intercept at the ordinate is due to a misadjustment of the voltmeter. Figure 25 shows the general results for five samples. Horizontal error bars gives the thickness range necessary to explain the variations in resistance assuming a constant resistivity. Vertical error bars show the range of resistivities using the crystal quartz thicknesses in calculations. Since the two voltage point-probes were approximately 1 mm apart, the maximum electric field was 0.5 Volt/cm whereas 10^3 Volt/cm would have been necessary to detect non-linearities due to porosity (see Chapter III). However, the low resistivity, close to the bulk vanadium resistivity, is an indication of the continuity of the film. Furthermore, some films show uniformity as no (or only minute) variations in resistivity were found.

5.7 Ellipsometry

Two types of ellipsometric measurements (or reflection interferometry¹) were carried out on a sample identical the one used for the electron microprobe measurements.

(a) First, at intervals of many hours starting immediately after bringing the film in contact with air, the growth of an oxide layer was observed. Results are given in Table VI(a). The different results at different angles of incidence (anisotropy) indicates a non flat surface.

¹For the theory of the Ellipsometer, see reference 20. see also reference 3, p. 520 for Reflection on Metals.

Some measurements done through the substrate on the back face of the film indicated a flat surface and no oxide layer.

(b) Then the film was etched along five lines (see Table VI for illustration) and multiple beam interferometry (or Fizeau interferometry) was used to measure the thickness. Results are given in Table VI(b) where t is the maximum variation in thickness along one line. Accuracy of the measurements was 100 \AA .

These tests confirm the results given earlier: The glass slides have an optically flat surface and the figures concerning the roughness of the film surface agree within a factor of 2 or less.

Some other conclusions can be drawn: The non oxidization of the substrate-film interface indicate that the cleaning procedure is efficient. Also a discrepancy is noticed between the crystal quartz thickness and the optically measured thickness. (Note that lines 1 and 5 have different thicknesses due to interference from the holder during the deposition).

CHAPTER VI

CONCLUSIONS

The production of good films is relatively easy. These can be described by the following list of characteristics.

(a) The microscope slides, cleaned according to methods explained previously, constitute very good substrate. The factory pre-polishing is sufficient for the needs of this experiment.

(b) High purity vanadium (or other material) film can be obtained.

(c) Films are relatively smooth. However, flatness could be probably be increased by heating the substrate.

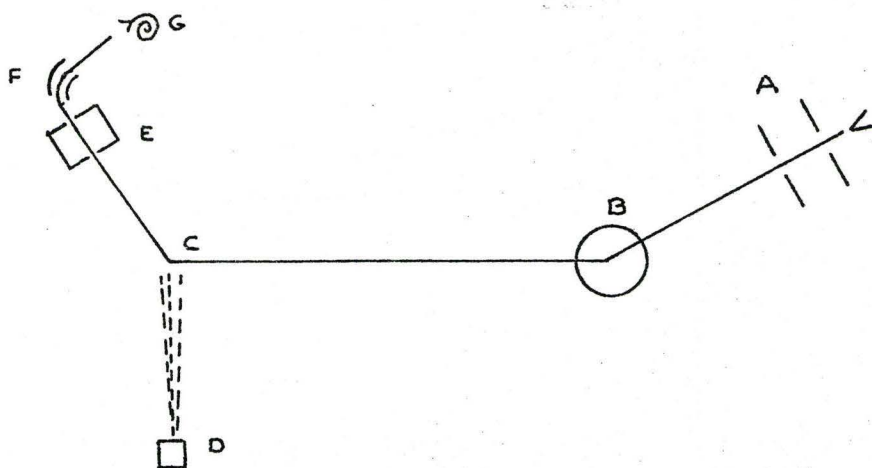
(d) The structure of the films remains constant despite variations in thickness, backing vacuum or deposition rate. Installation of a shutter would provide the possibility of producing thin, very fast deposited films.

BIBLIOGRAPHY

1. Allen, J.A., Evan, C.C. and J.W. Mitchell. Structure and Properties of Thin Films. (Neugebauer, Newkirk and Vermibyca). New York: John Wiley and Sons, (1959).
2. Appleyard, E.T.S. and A.C.B. Lovell. Proc. Roy. Soc., A158, 718, (1937).
3. Basset, G.A. Phil. Mag., 3, 1042, (1958).
4. Basset, G.A., Menter, J.W. and D.W. Parkley. Structure and Properties of Thin Films. (Neugebauer, Newkirk and Vermibyca). New York: John Wiley and Sons, (1959).
5. Chopra, K.L. Appl. Phys. Lett., 7, 140, (1965).
6. Chopra, K.L. J. Appl. Phys., 37, 2249, (1966).
7. Chopra, K.L. and M.R. Randlett, J. Appl. Phys., 9, 402, (1966) and 39, 1874, (1968).
8. Chopra, K.L. Thin Film Phenomena. New York: McGraw Hill, (1969).
9. Fray, A.F. et al. Brit. Jour. Appl. Phys., 10, 332, (1959).
10. Heidenreich, R.D. Fundamental of Transmission Electron Microscopy. New York: John Wiley & Sons, (1964).
11. Holland, L. Vacuum Deposition of Thin Films. New York: Chapman and Hall, (1963).
12. Holland, L. The Properties of Glass Surface. New York: John Wiley & Sons, (1964).
13. Jenkins, F. and H. White. "Fundamentals of Optics". New York: McGraw Hill, (1957).
14. Kaelble, E. "Handbook of X-rays". New York: McGraw Hill, (1967).
15. O'Connor, T.L. and H.H. Urling. J. Phys. Chem., 61, 402, (1957).
16. Pashley, D.W. Adv. Phys., 14, 361, (1965).
17. Poppa, H. J. Appl. Phys., 38, 3883, (1967).

18. Putner, T. Brit. Jour. Appl. Phys., 10, 332, (1959).
19. Rhodin, T.N., Orr, W.H. and D. Walter. Mémoires Scien. Rev. Metallurg., LXVII, 65, (1965).
20. Rowe, E.C. M.Sc. Thesis. McMaster University, (1968).
21. Sze, S.M. "Physics of Semiconductor Devices". New York: John Wiley & Sons, (1969).

FIG 1 : SCHEMATIC DIAGRAM OF THE COMPLETE SYSTEM



A : Accelerating Voltage

B : Analysing Magnet

C : Thin Film Target

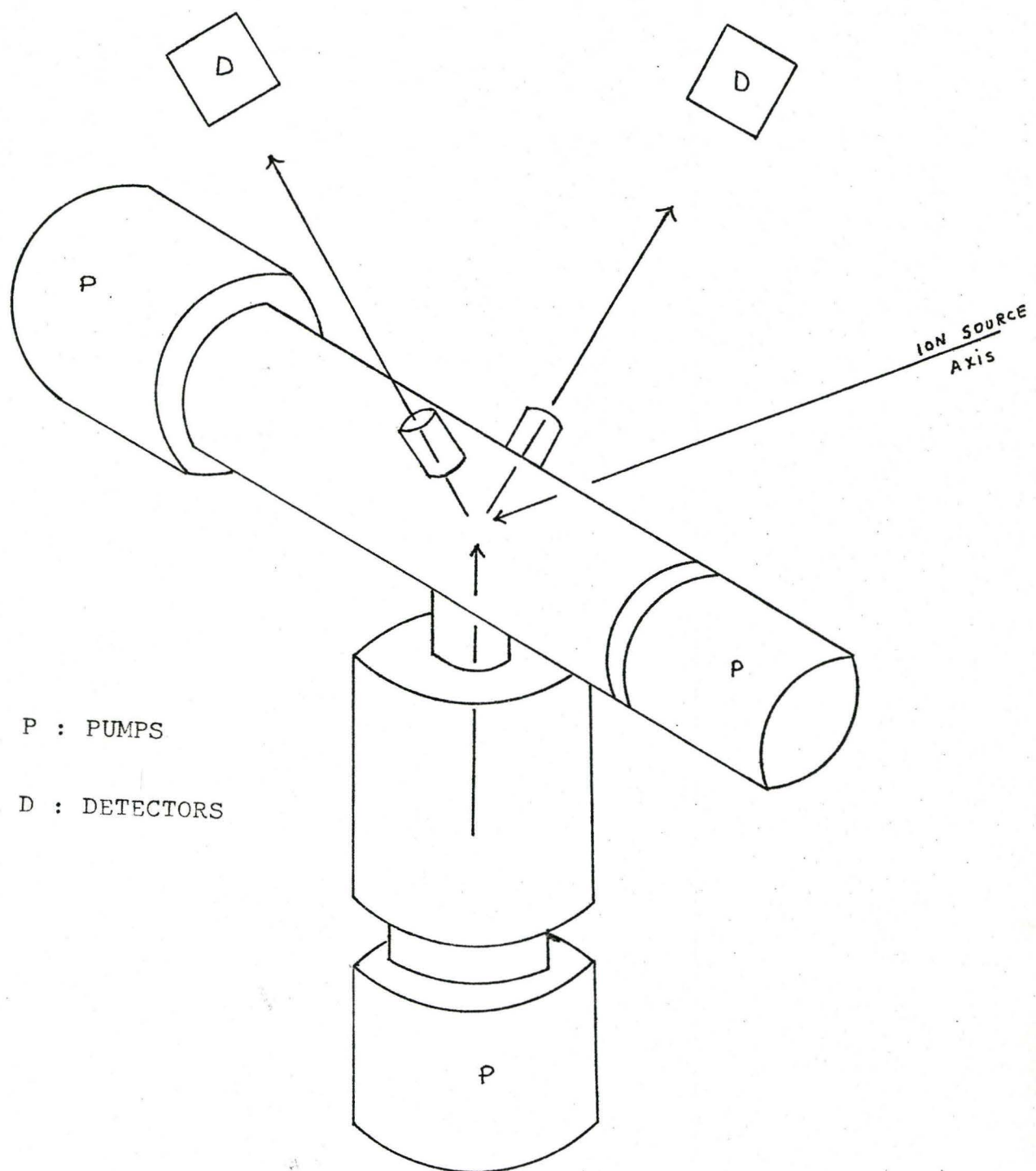
D : Electron-gun Evaporator

E : Charge Exchange Chamber

F : Electrostatic Analysing Plates

G : Channeltron

FIG 2 : 3-D VIEW OF EVAPORATION AND TARGET CHAMBERS



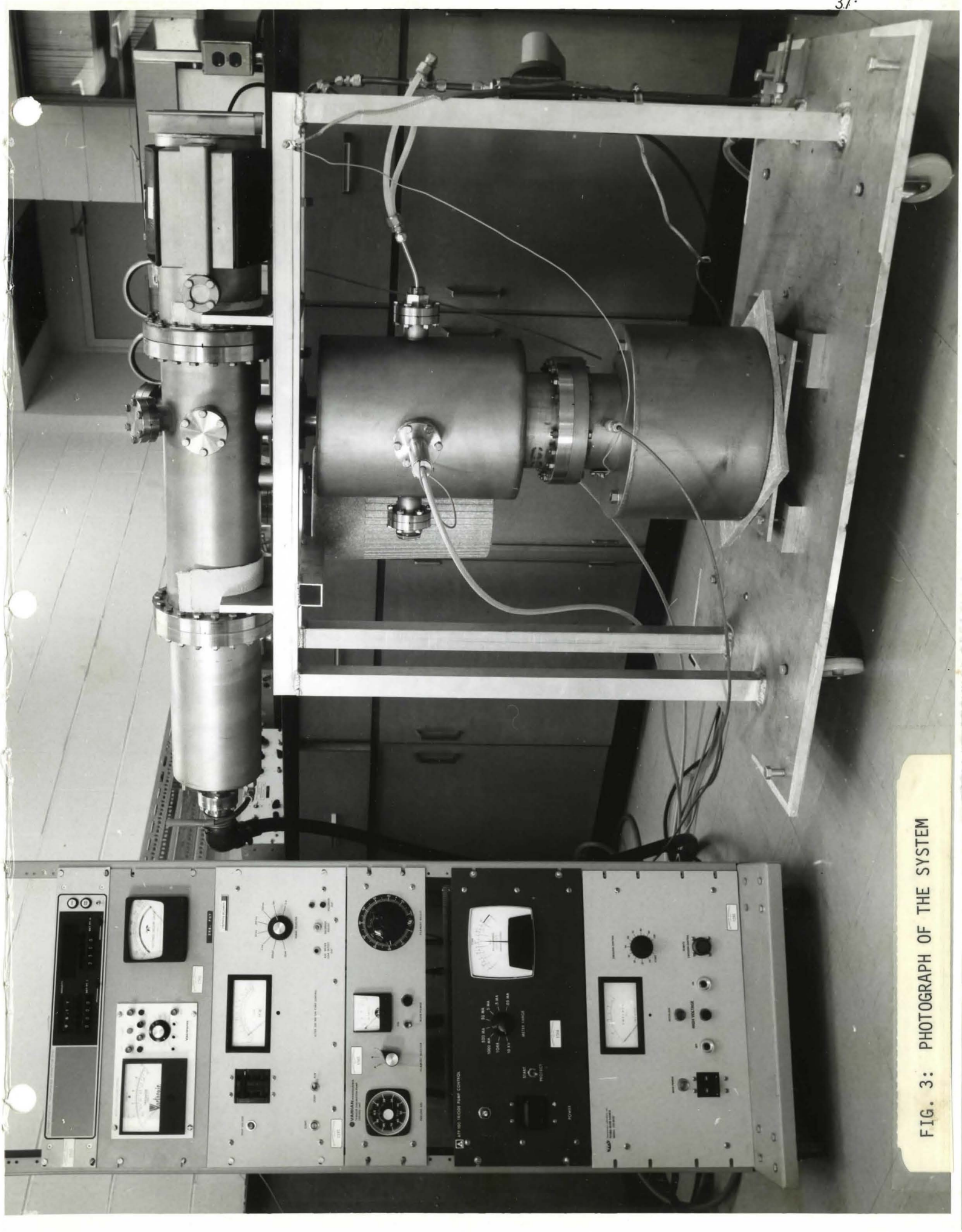


FIG. 3: PHOTOGRAPH OF THE SYSTEM

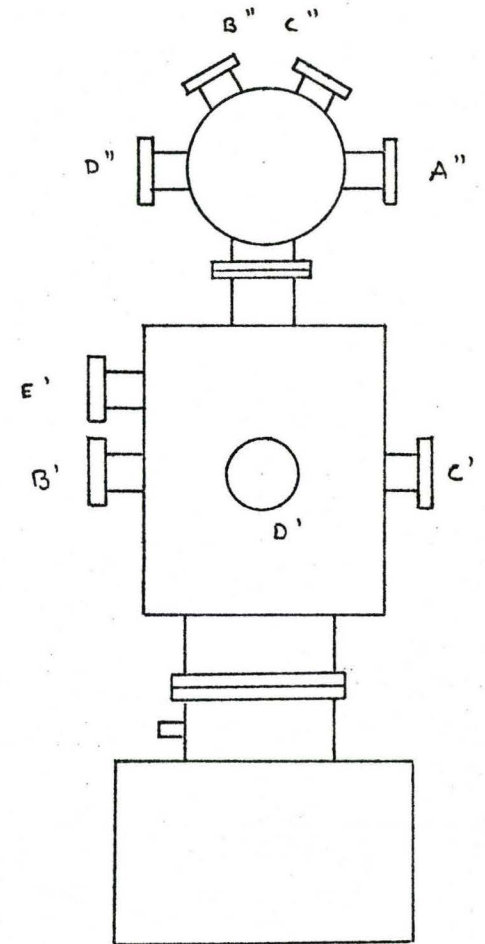
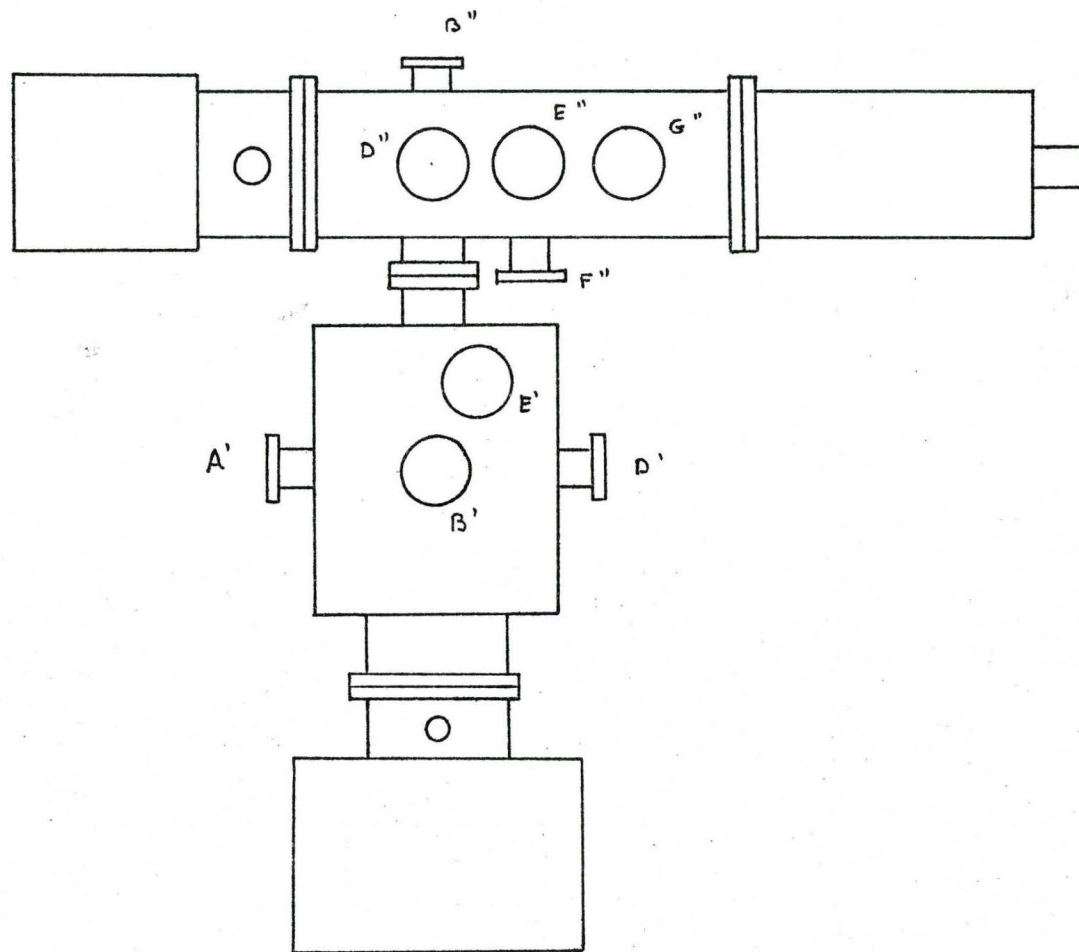
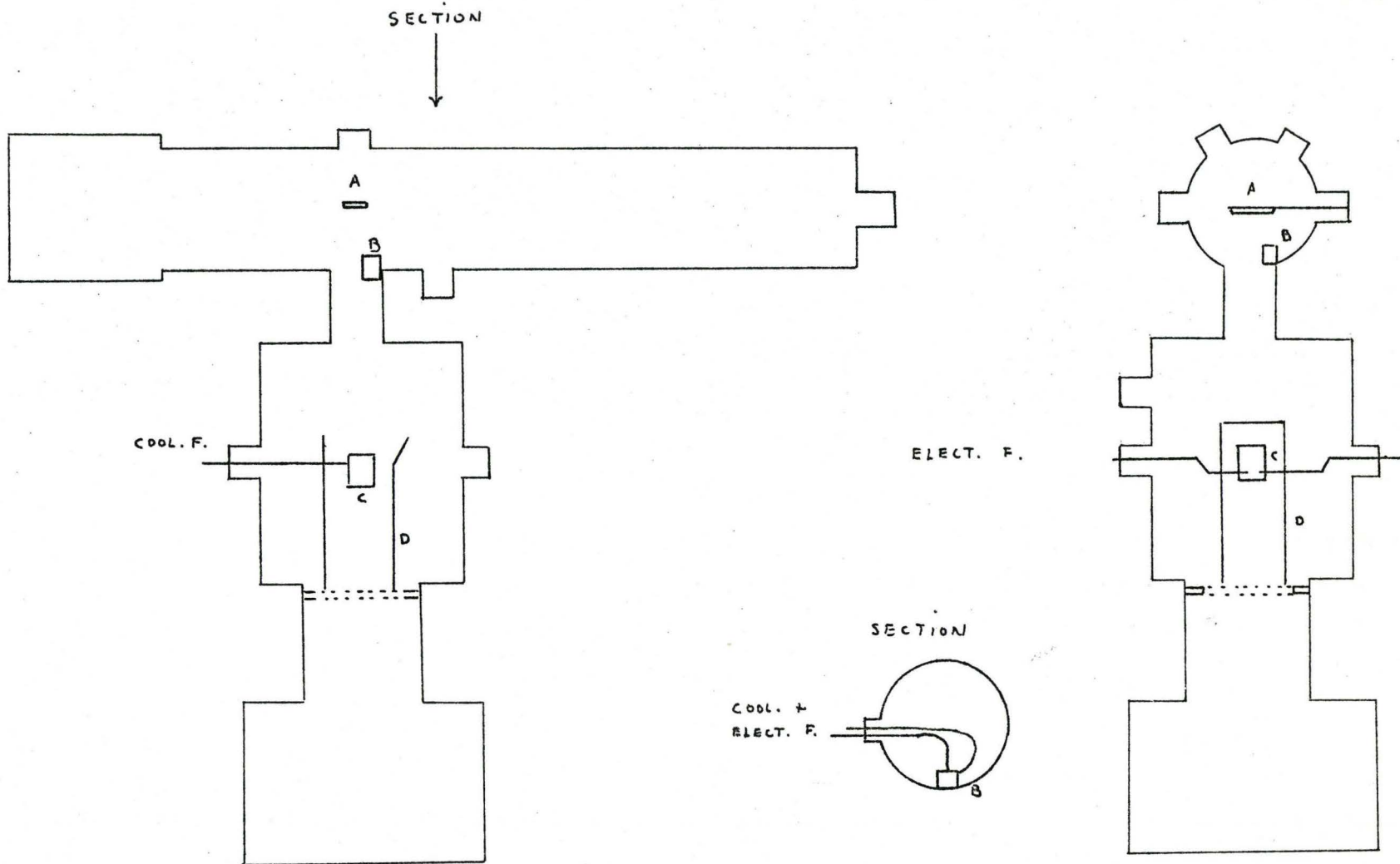


FIG 4 : EXTERNAL ASPECT OF EVAPORATOR-TARGET ARRANGEMENT



- | | |
|------------------------------------|-----------------------------|
| COOL. F. : Feedthrough for coolant | B : Thickness monitor head |
| ELECT. F. : Electrical feedthrough | C : Electron-gun evaporator |
| A : Substrate holder | D : Vapour shield |

FIG 5: INTERNAL ASPECT OF THE SYSTEM

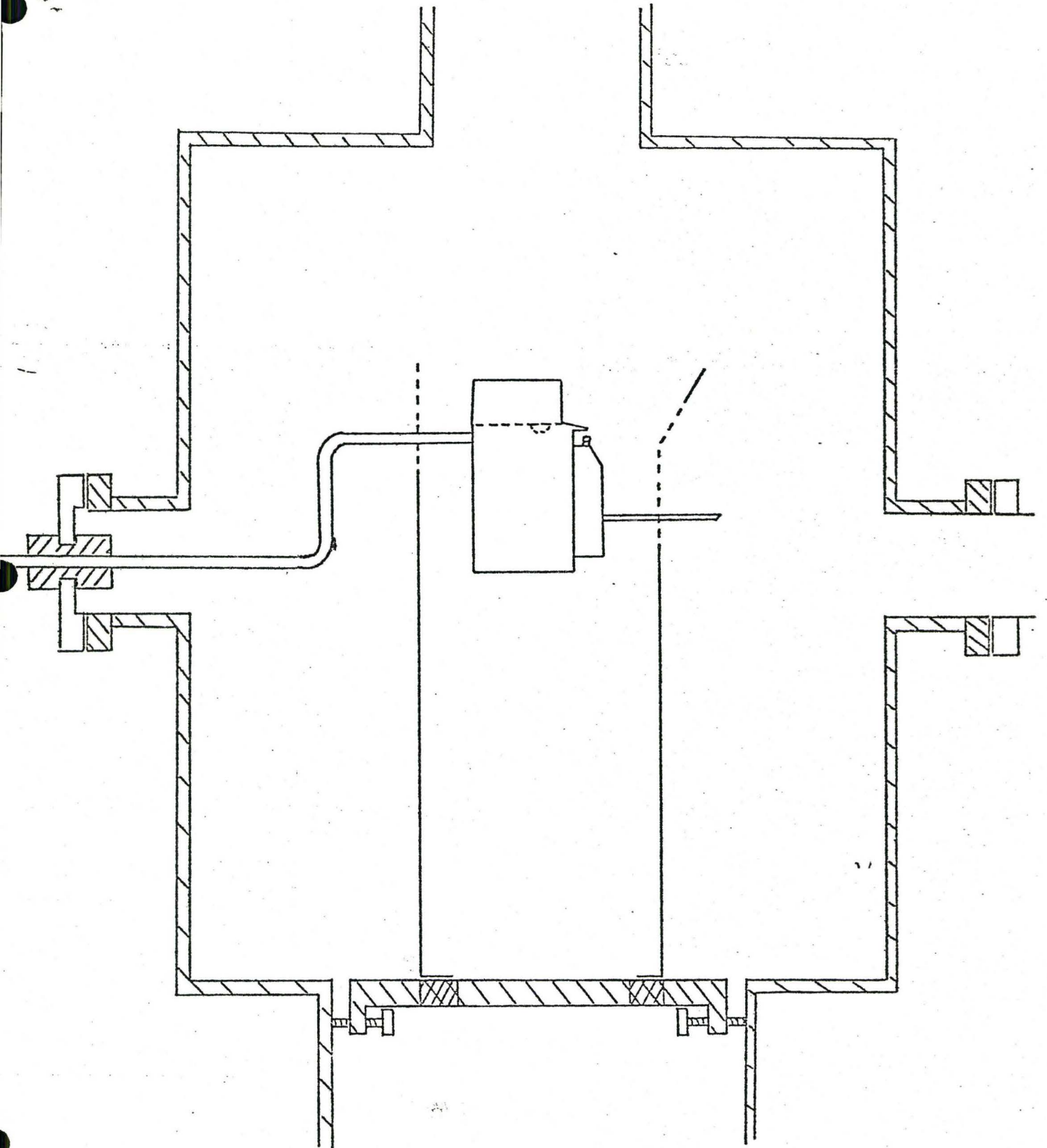
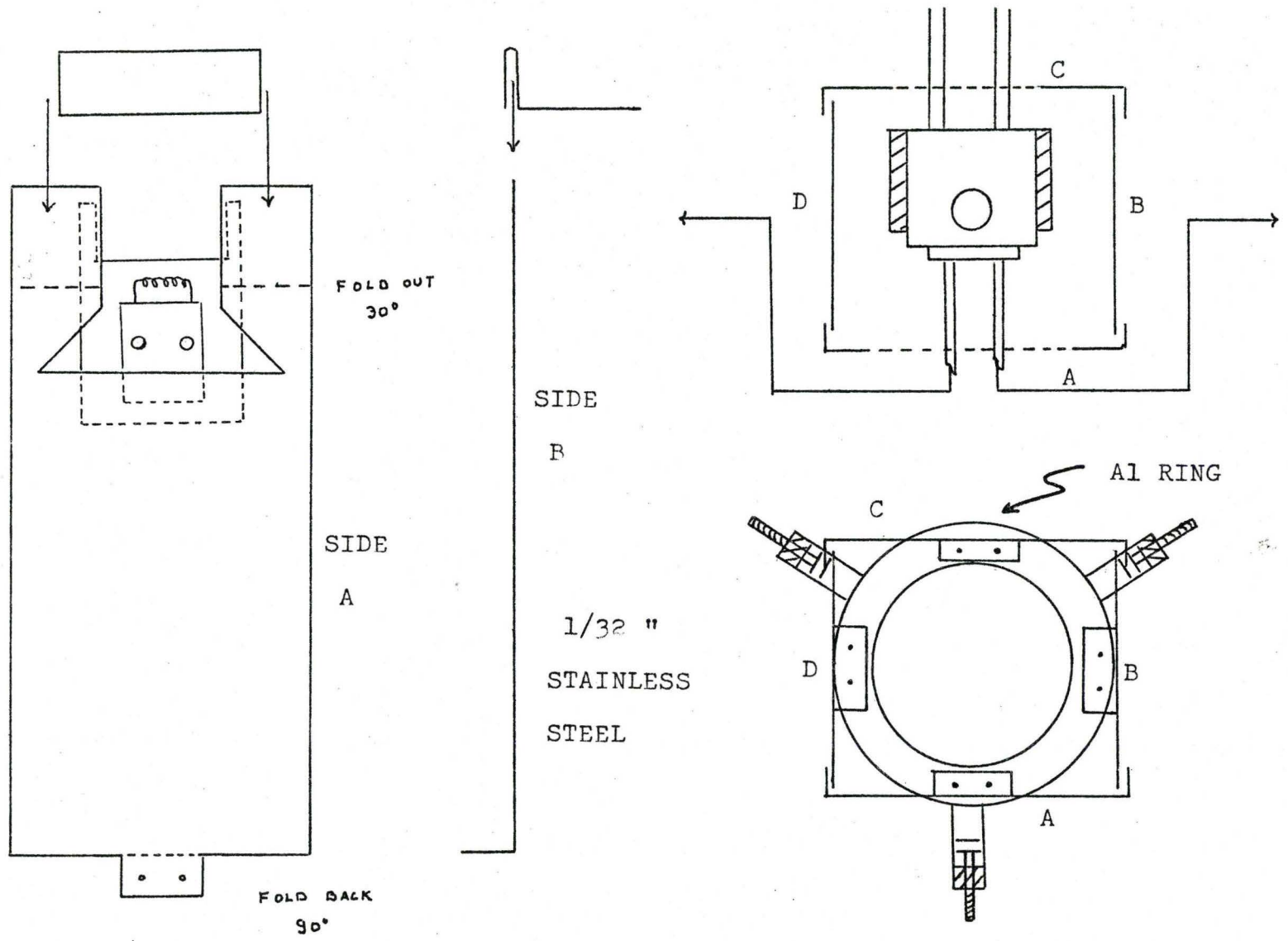


FIG 6 : EVAPORATION CHAMBER

FIG 7 : METAL VAPOUR SHIELD



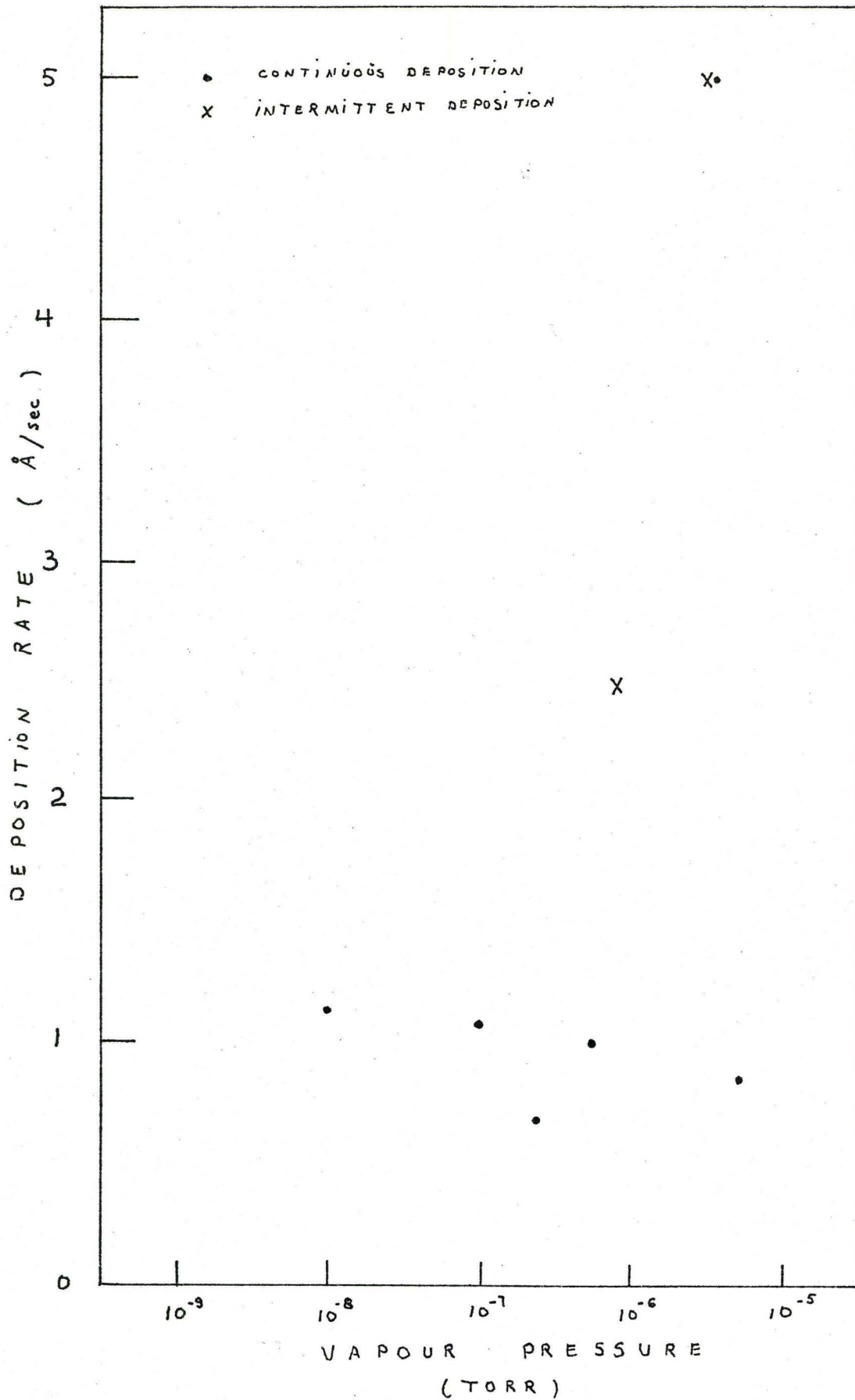
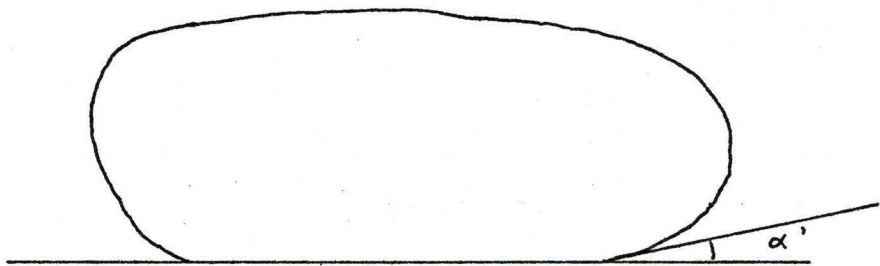
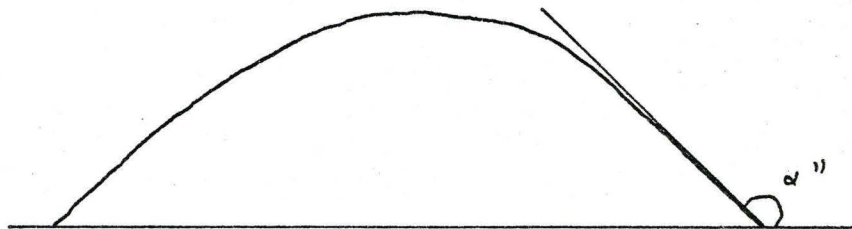


FIG 8 : DEPOSITION RATE vs VAPOUR PRESSURE

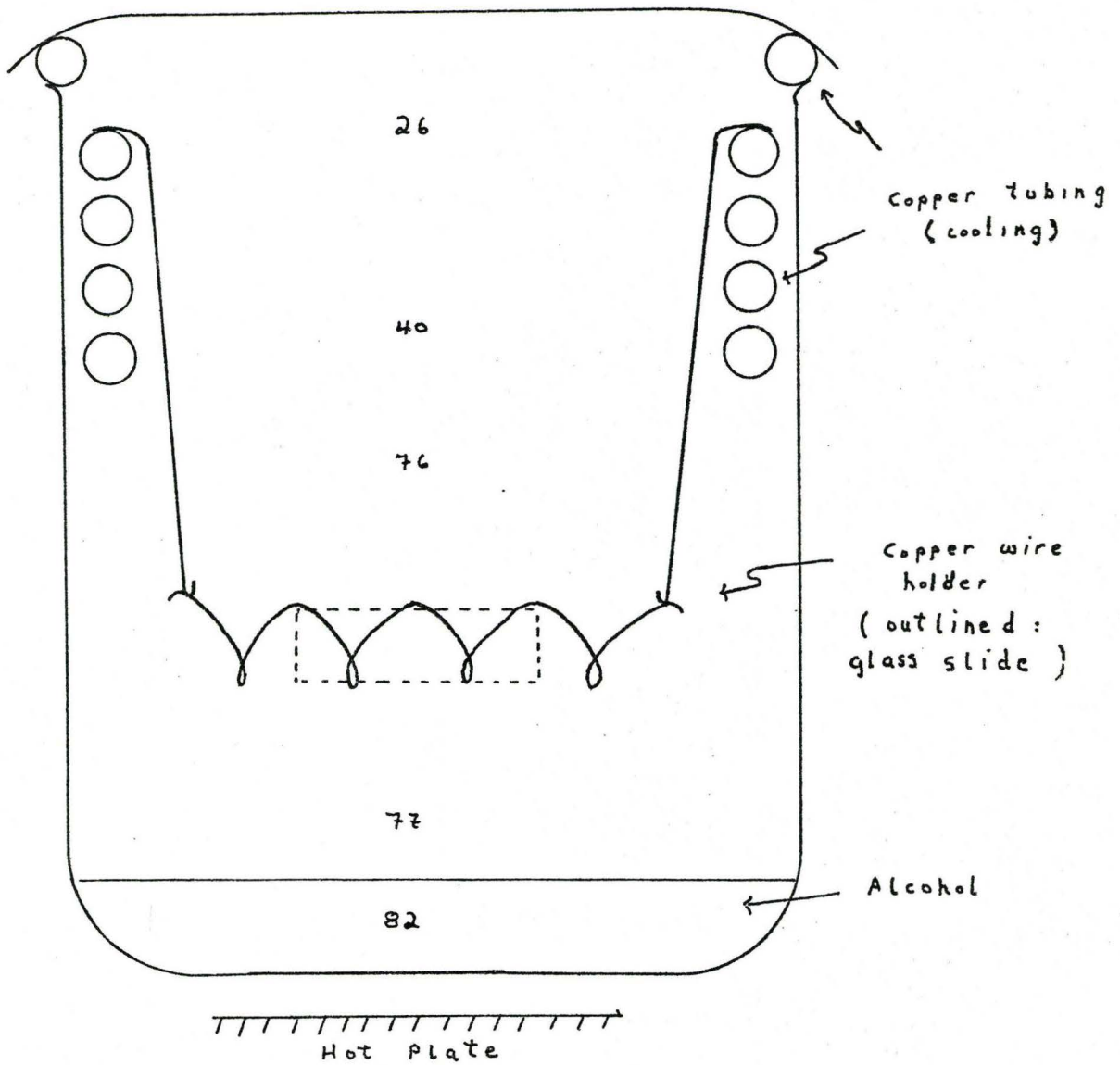


a) Bad Wetting



b) Good Wetting on a Very Clean Glass Surface

FIG 9 : EXTERNAL CONTACT ANGLE OF WATER DROPS ON GLASS SURFACE



Numbers are Temperatures ($^{\circ}\text{C}$)

FIG 10 : APPARATUS FOR CLEANING GLASS SLIDES IN ALCOHOL VAPOUR

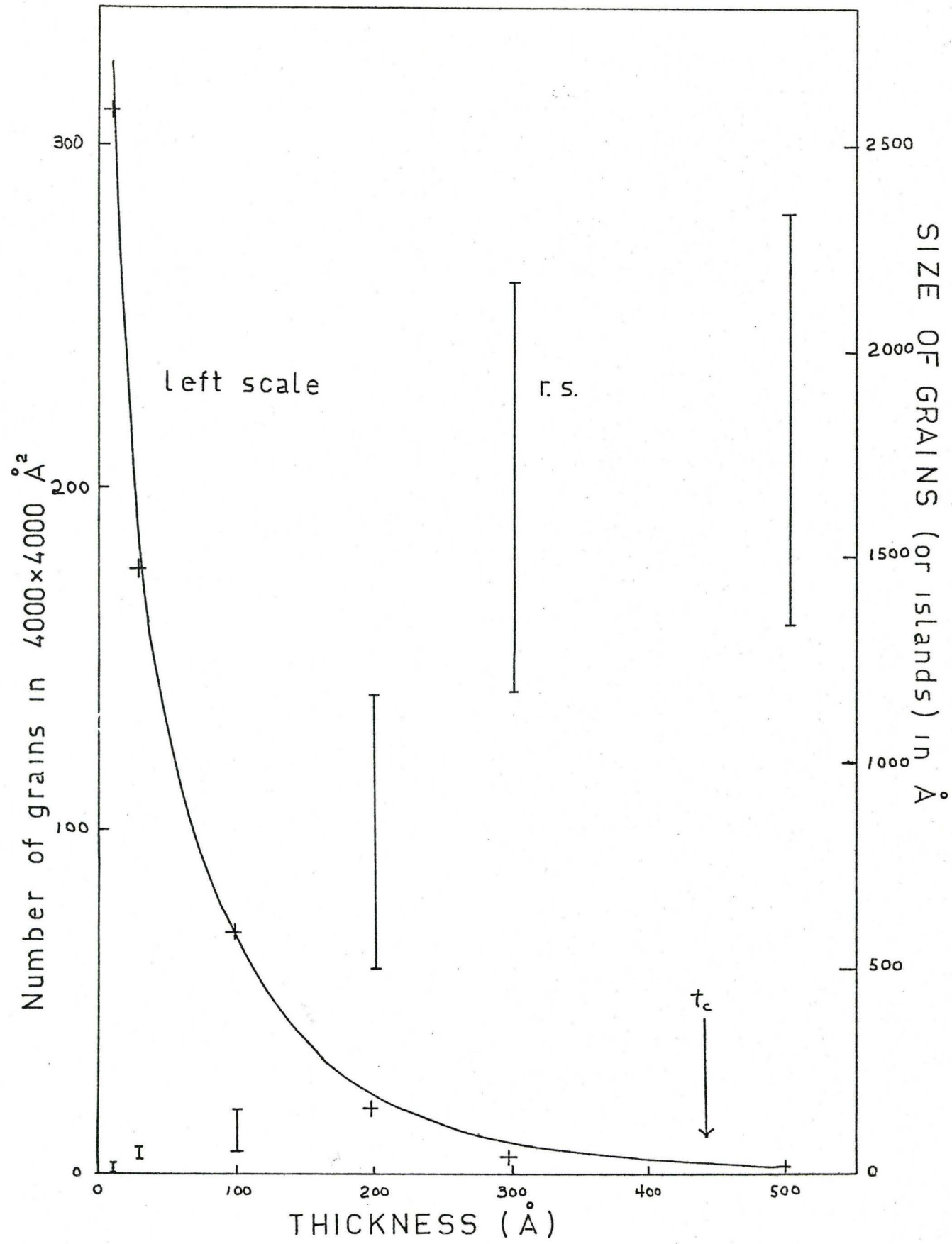
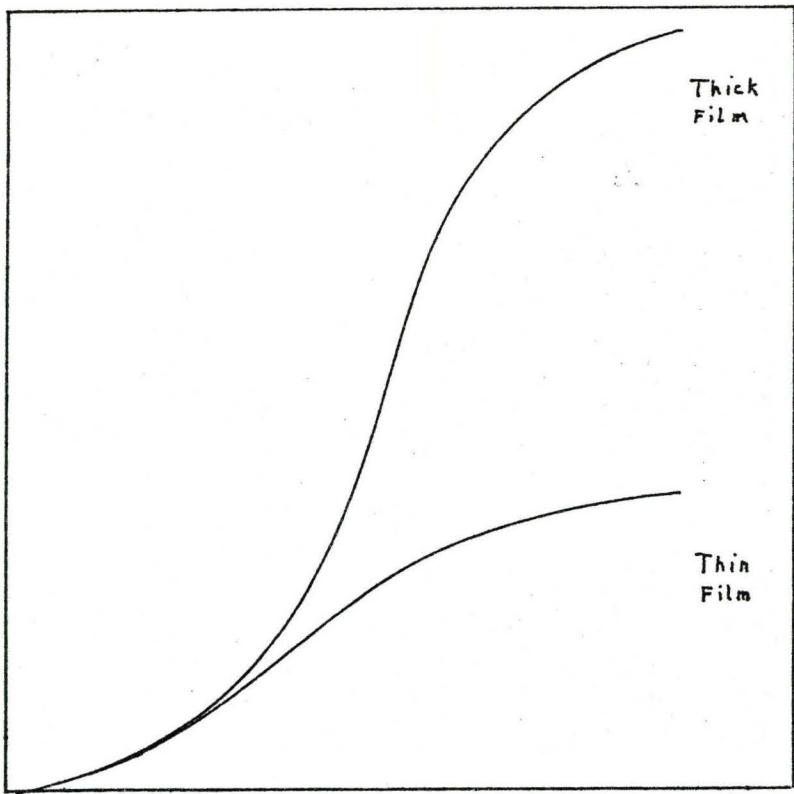


FIG 11 : NUMBER DENSITY OF GRAINS vs THICKNESS

(a)

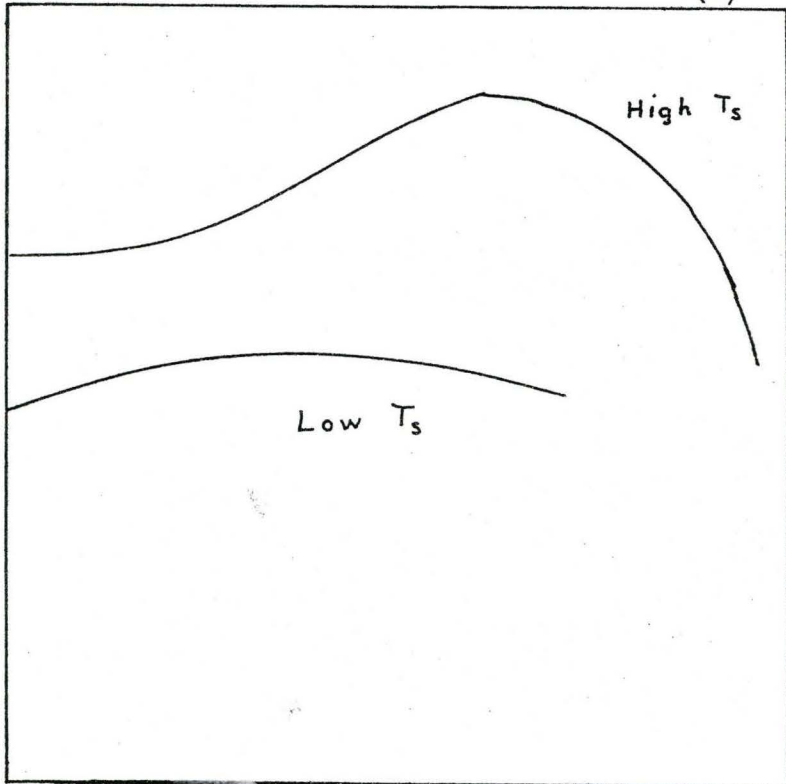
GRAIN SIZE



SUBSTRATE TEMPERATURE

(b)

GRAIN SIZE



DEPOSITION RATE

FIG 12 (a) (b)

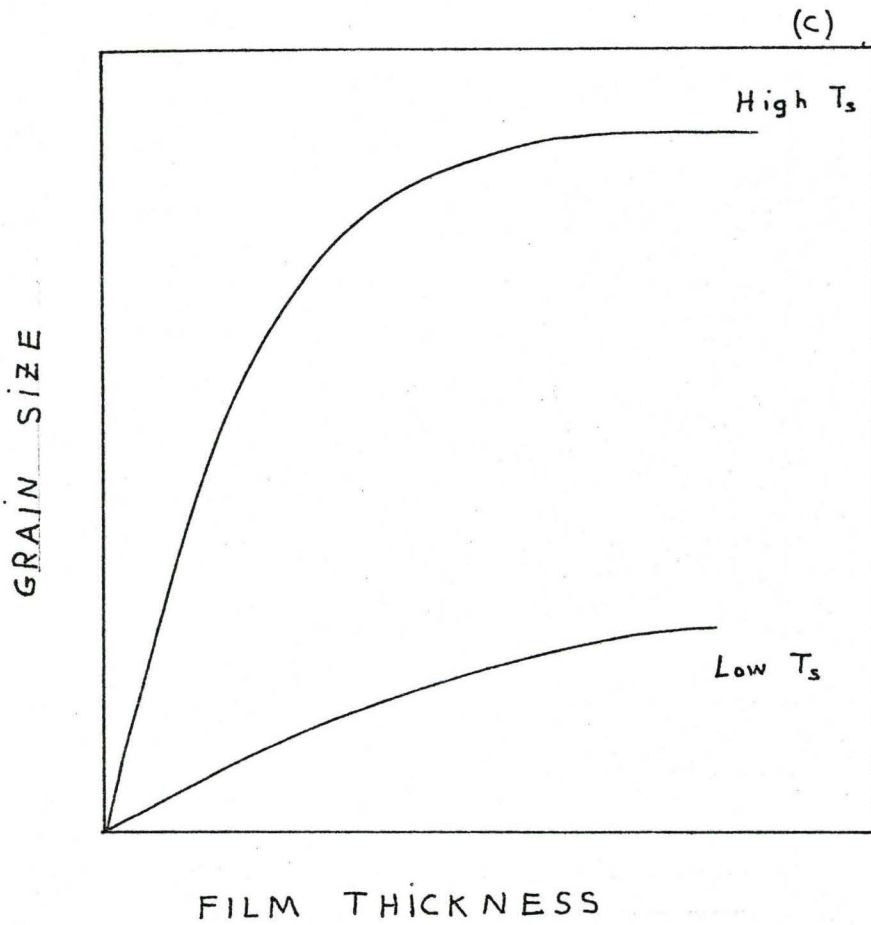


FIG 10 (c)

EFFECT OF VARIOUS PARAMETERS ON GRAIN SIZE

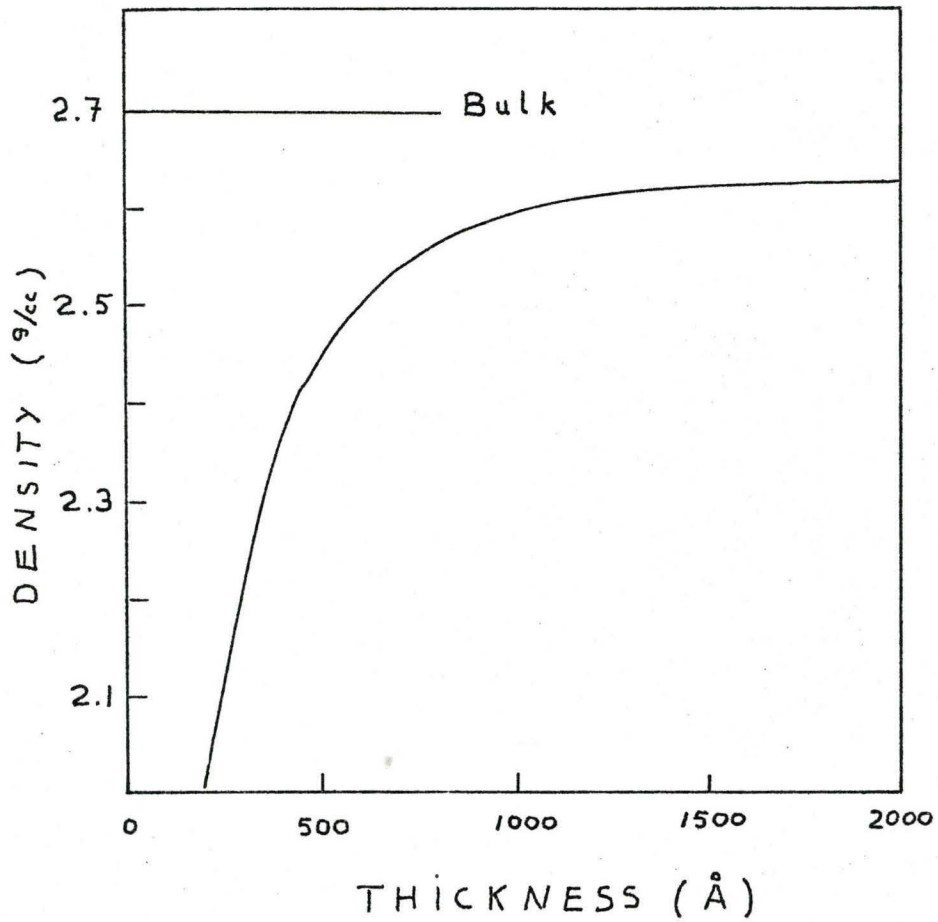


FIG 1² : DENSITY OF VANADIUM FILM
vs THICKNESS

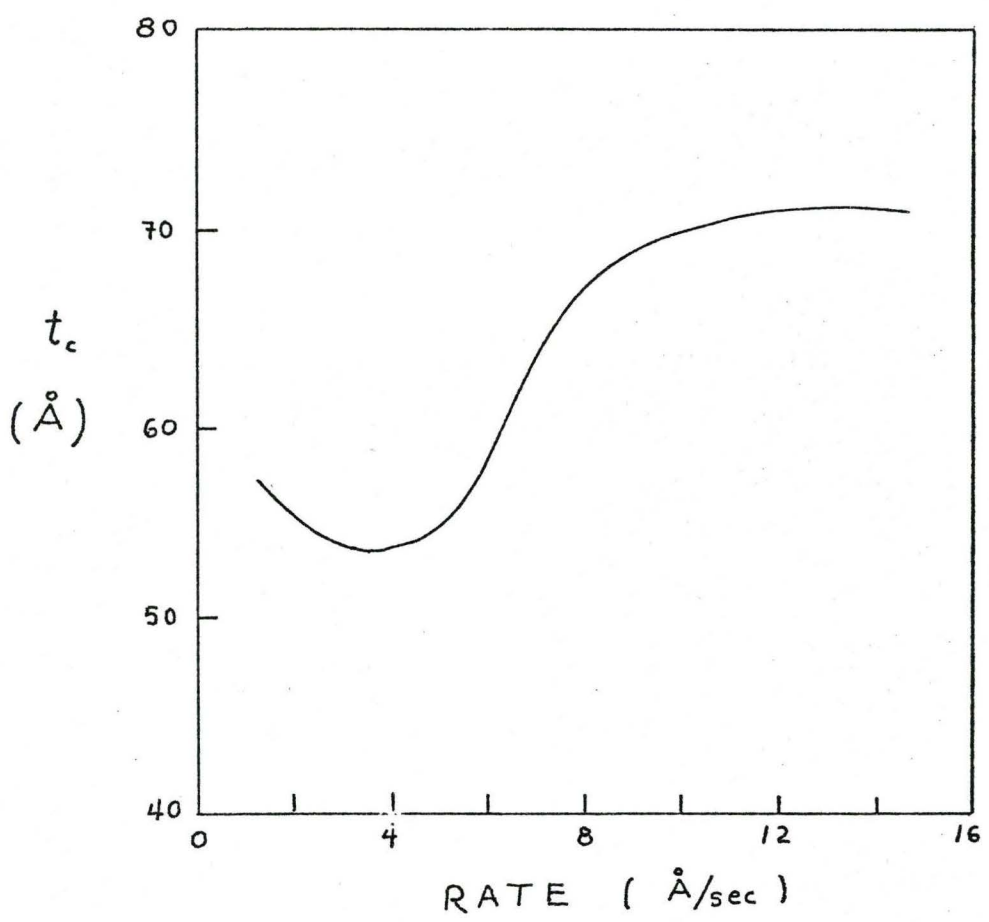


FIG 14 : CRITICAL THICKNESS vs DEPOSITION RATE

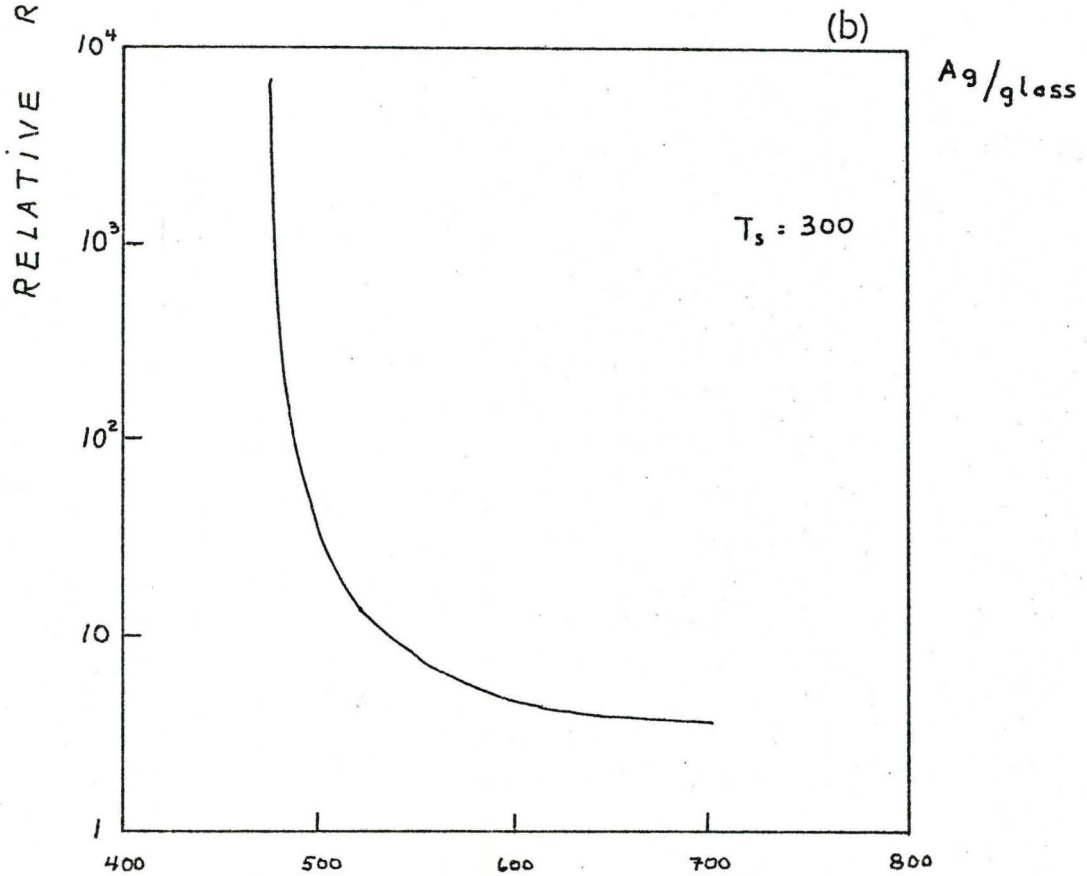
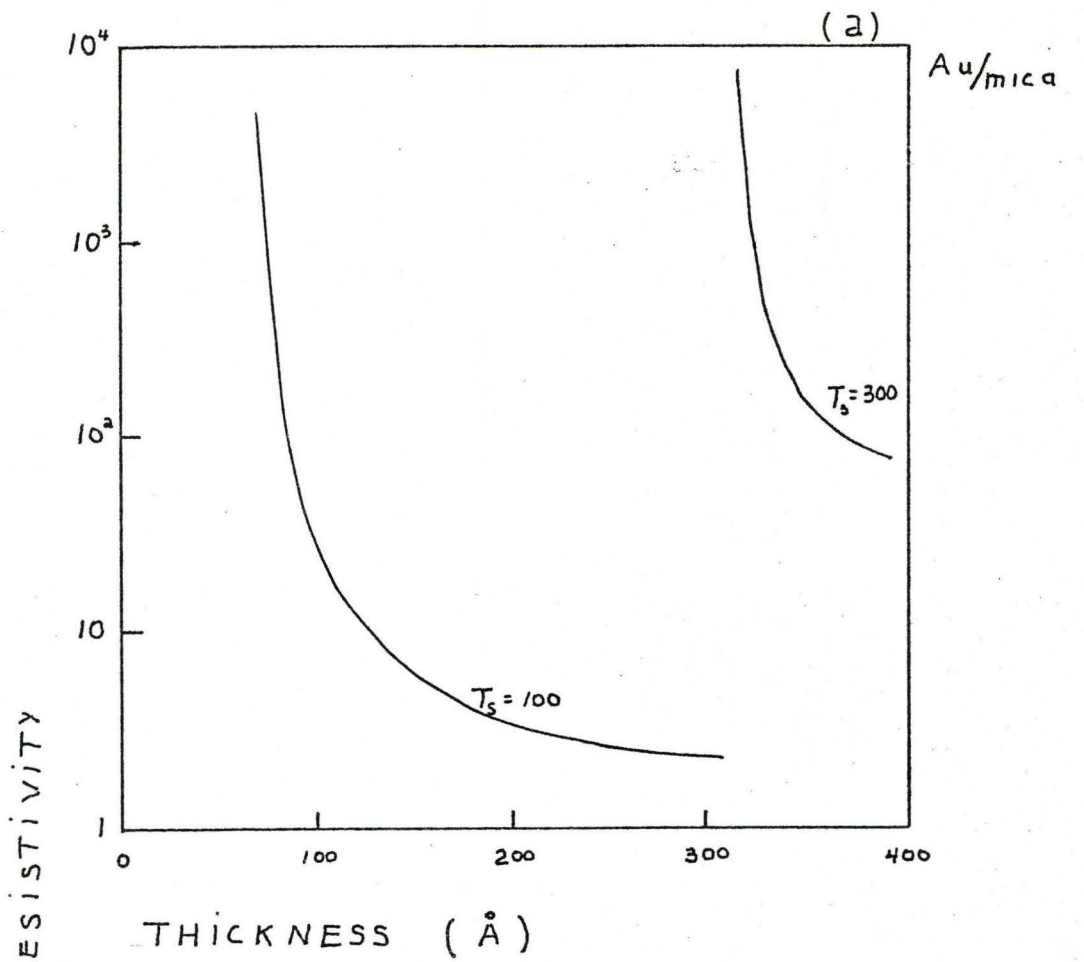


FIG 15 (a) (b)

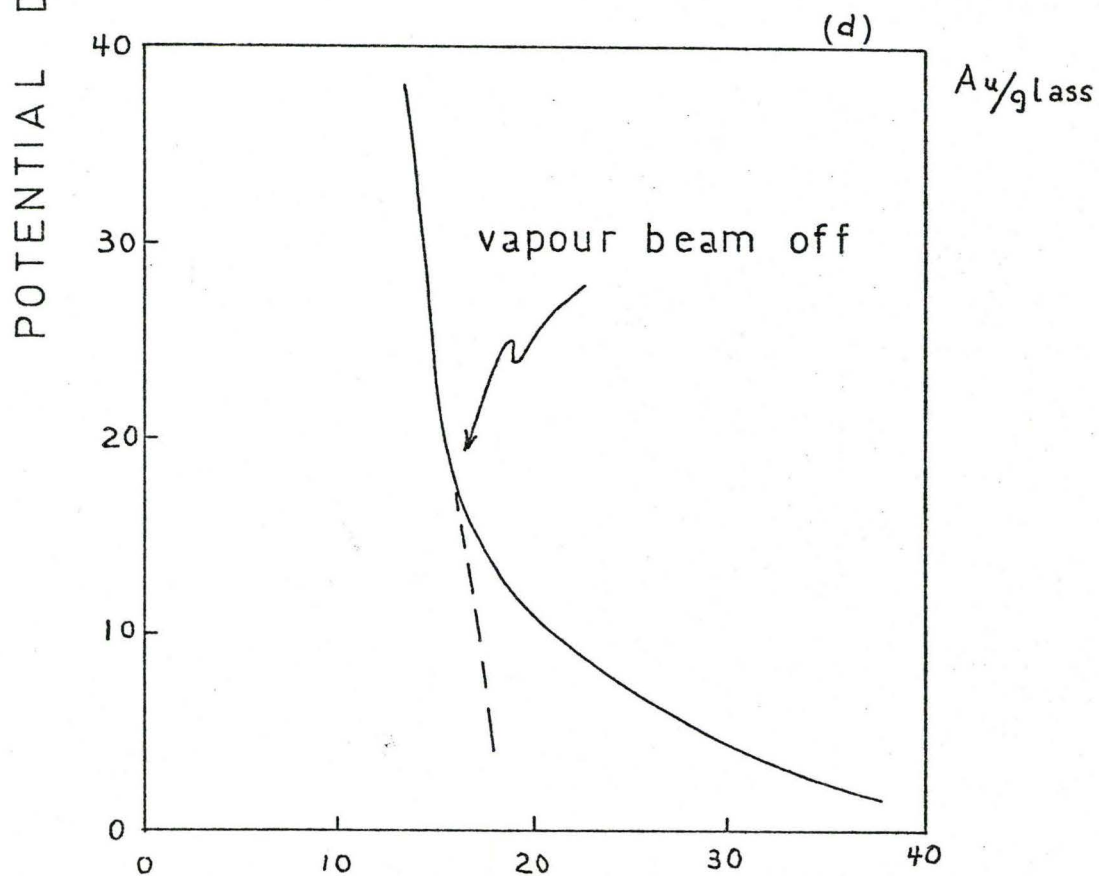
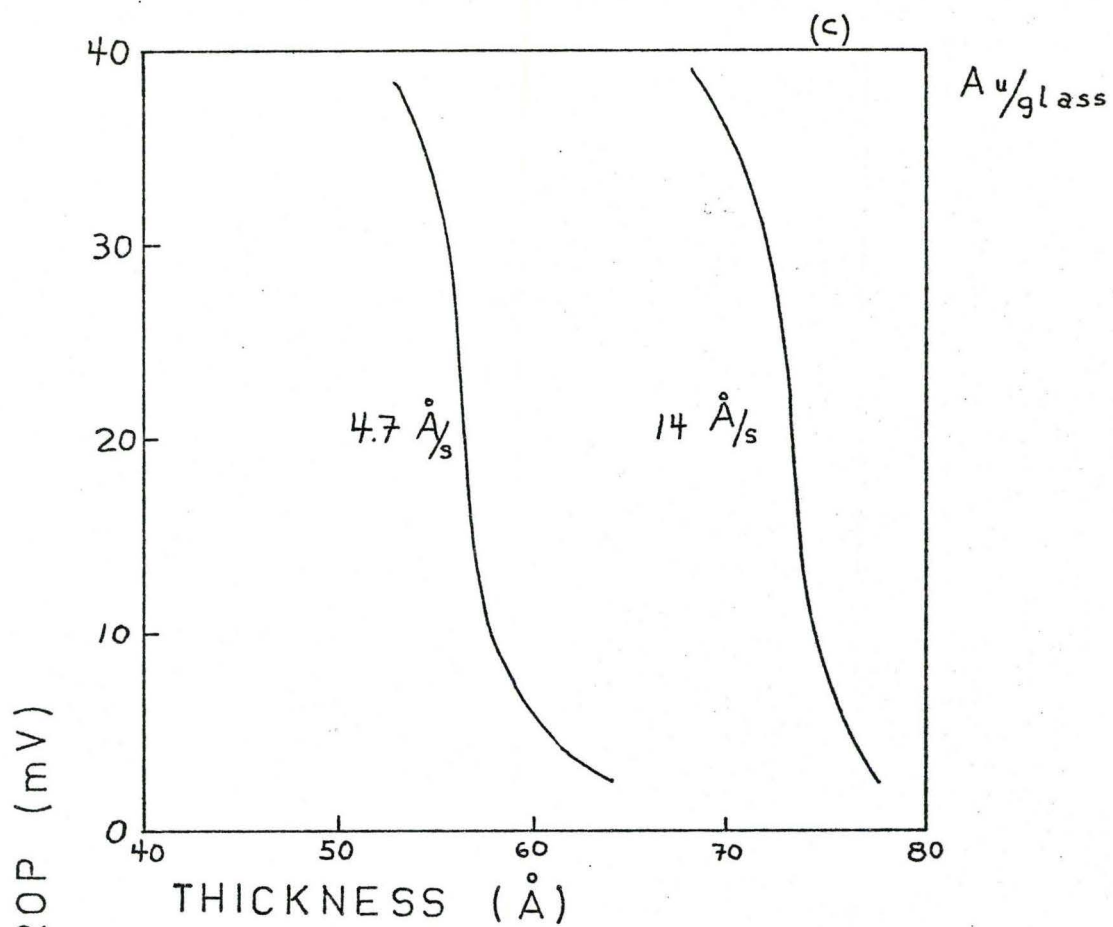


FIG. 15 (c) (d): EFFECT OF INCREASING THICKNESS ON RESISTIVITY

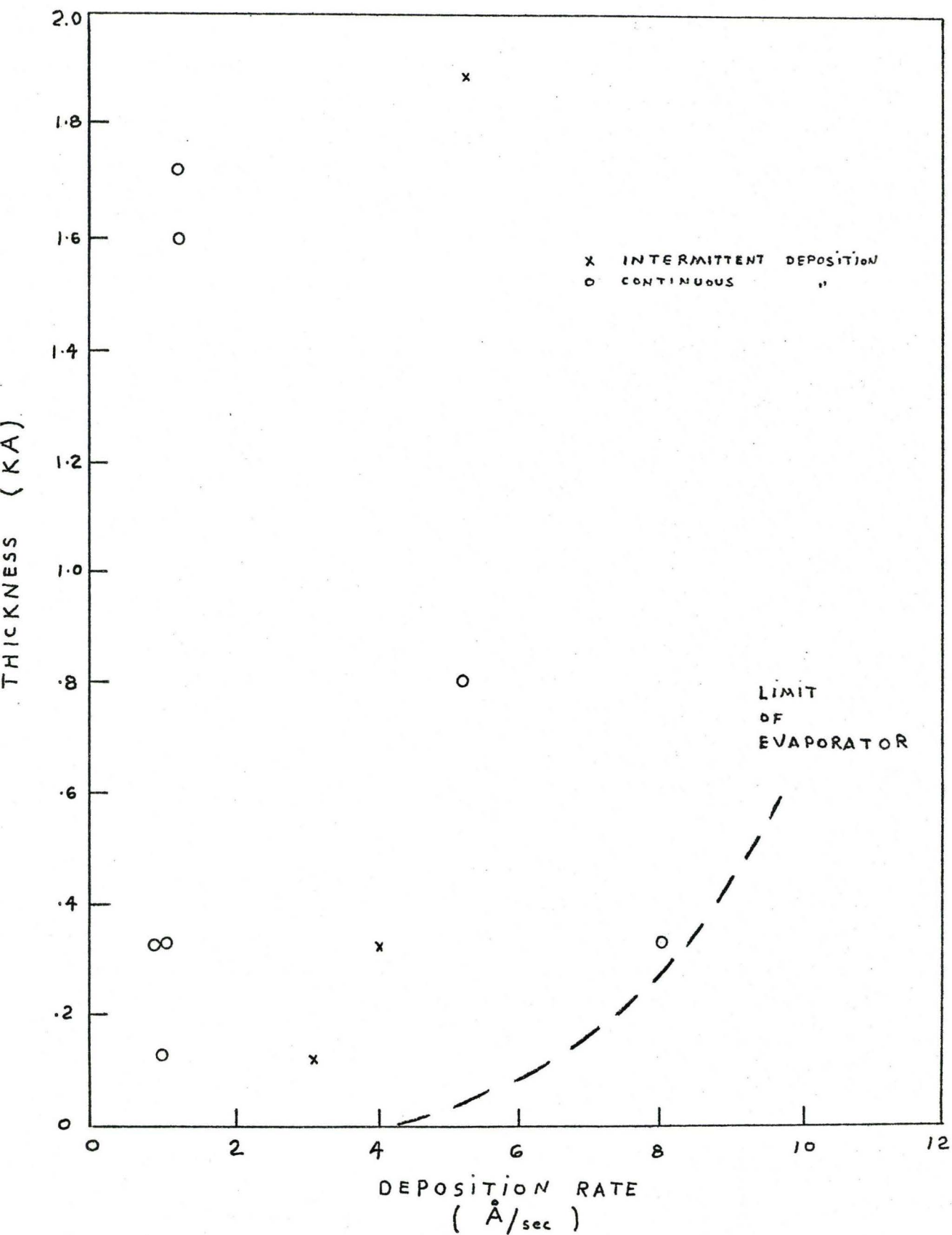


FIG. 16 PARAMETERS OF SAMPLES

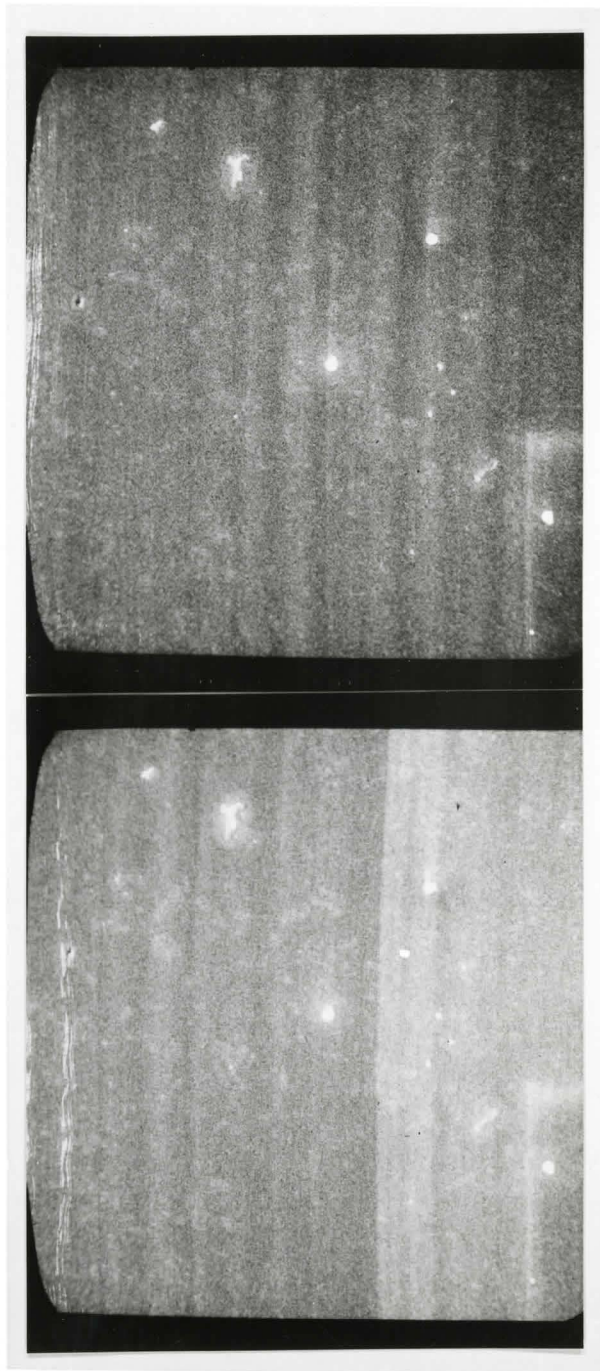
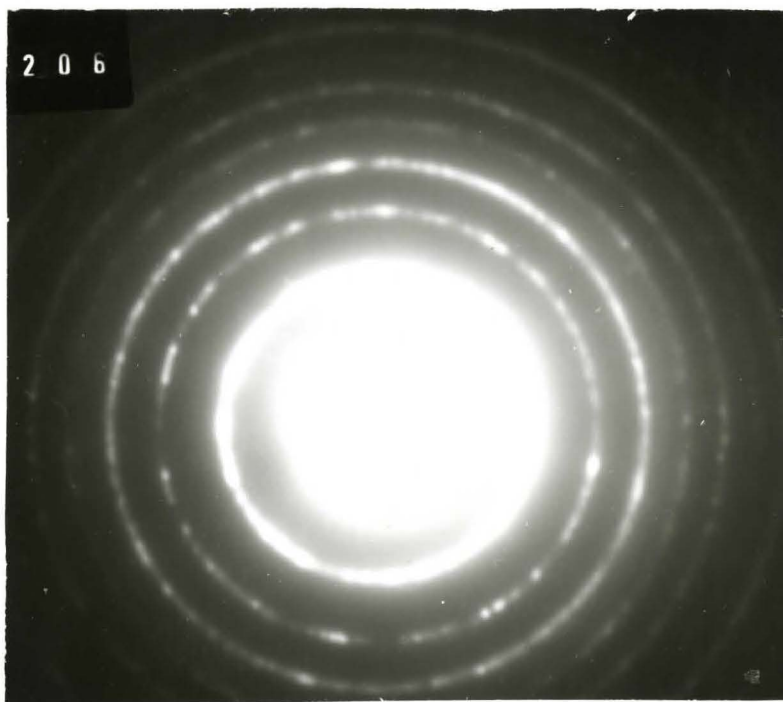
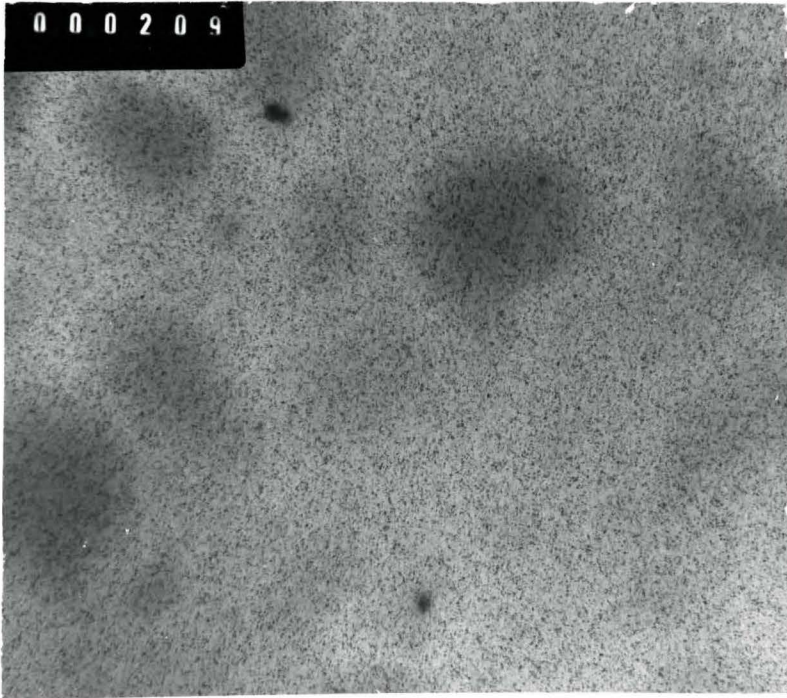


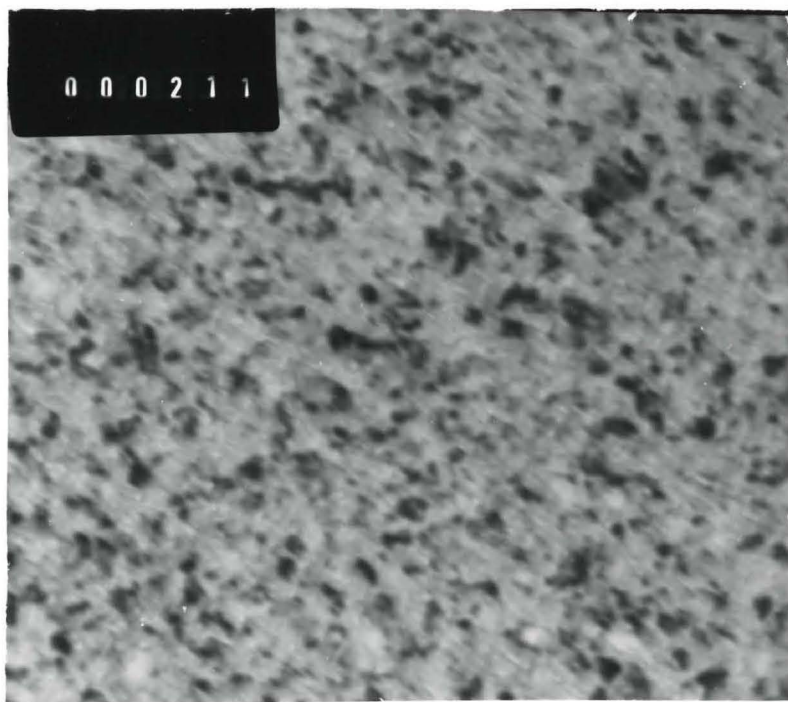
FIG 17

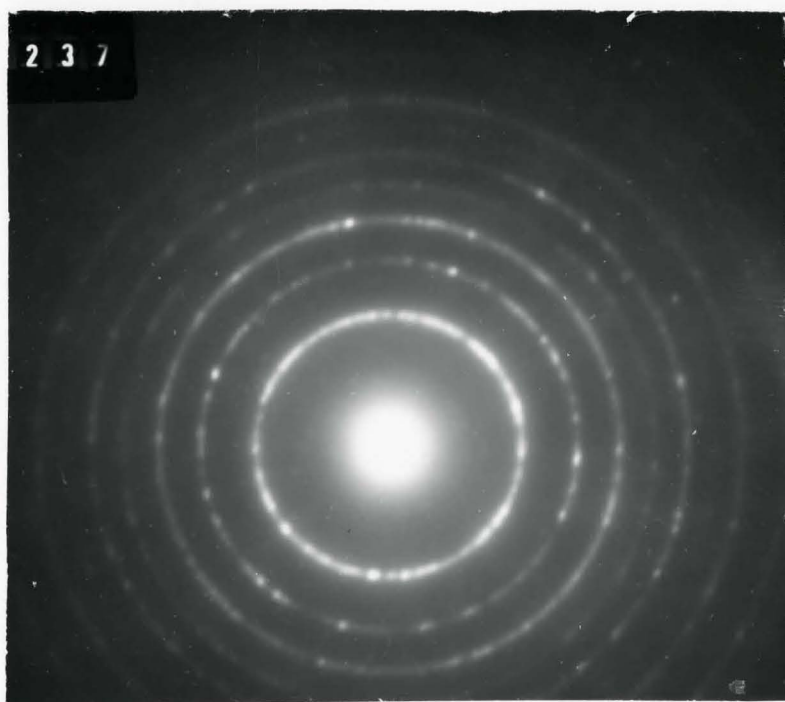
FIG. 18: ELECTRON MICROGRAPHS AND CORRESPONDING DIFFRACTOGRAPHS

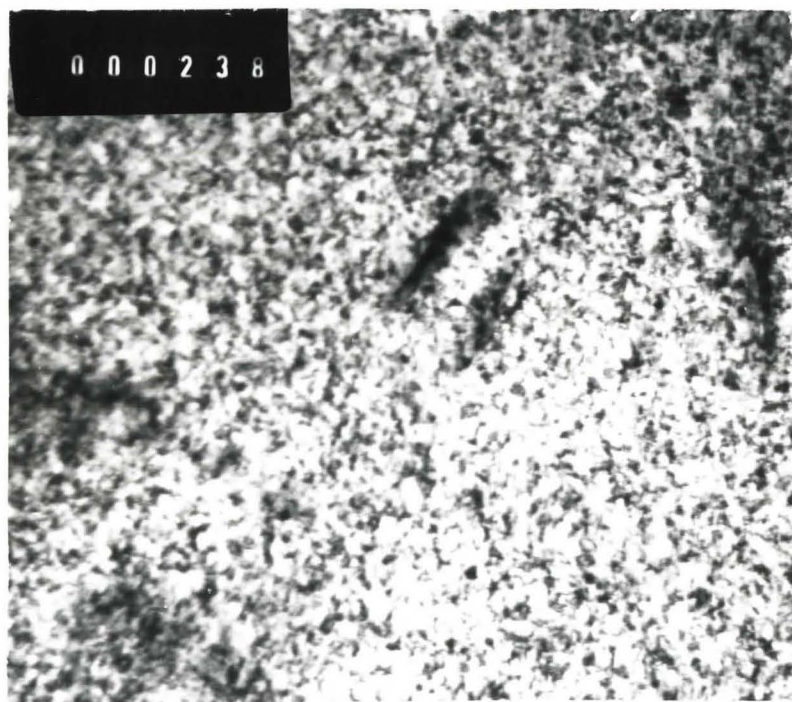
- Picture Number: 206 Transmission diffraction pattern
(Thickness = 335 A)
- 209 Micrograph 16500 X
(Thickness = 335 A)
- 211 Micrograph 93000 X
- 237 Transmission diffraction pattern
(Thickness = 1592 A)
- 238 Micrograph 64000 X
(Thickness = 1592 A)
- 260 Reflection diffraction pattern
(Thickness = 1725 A)

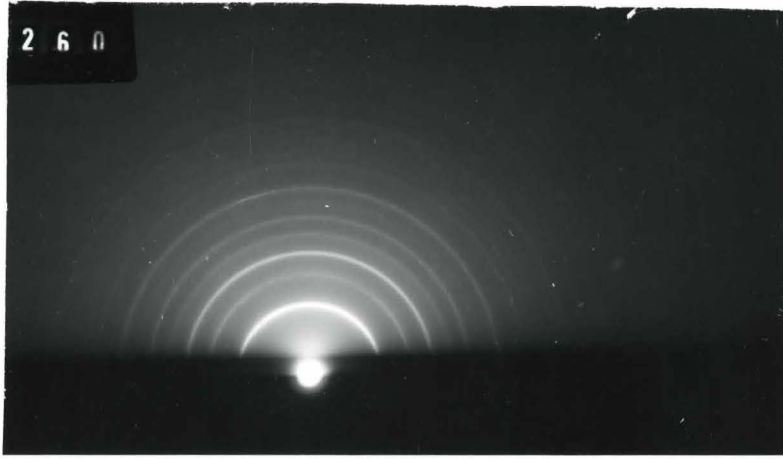












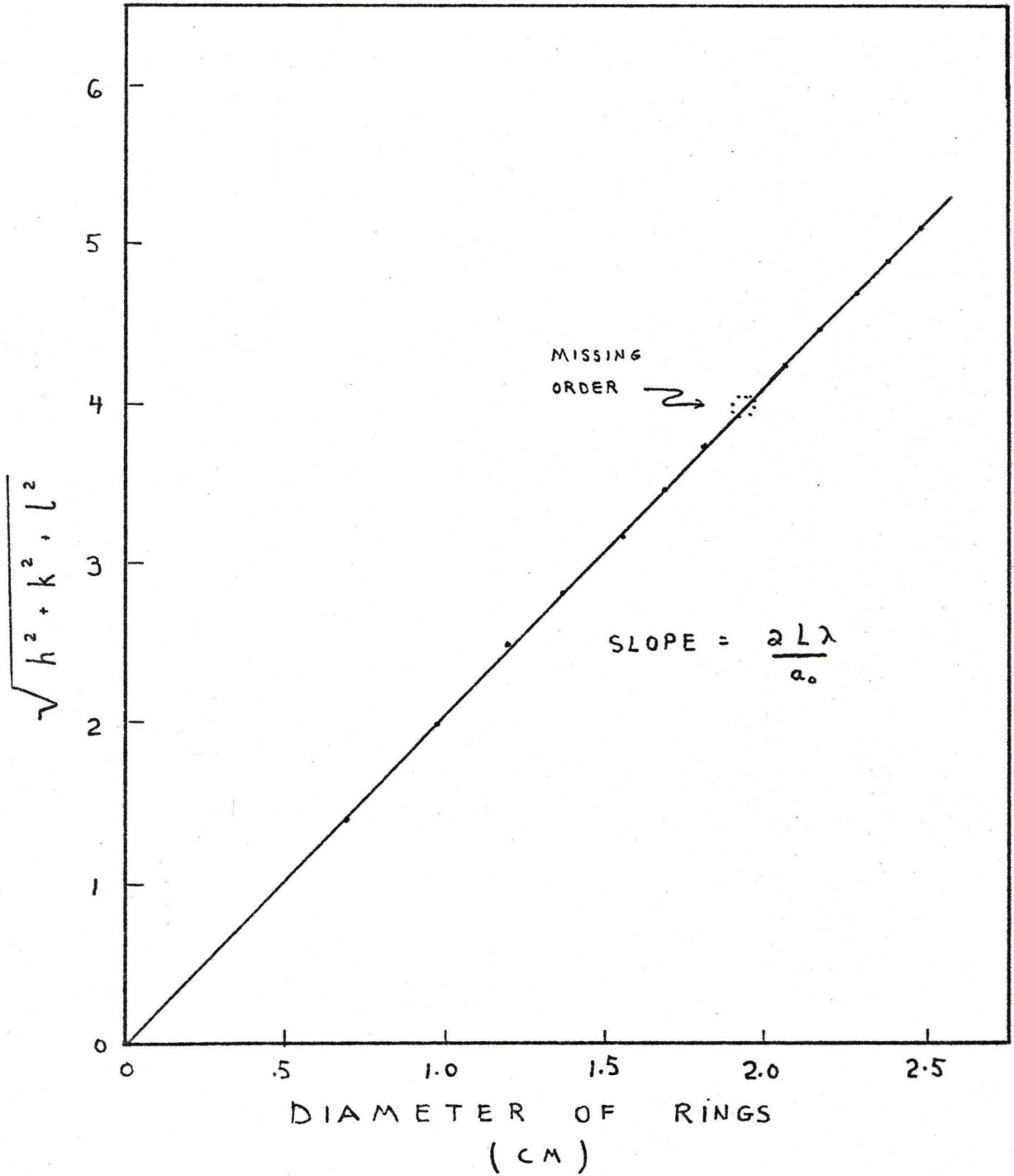
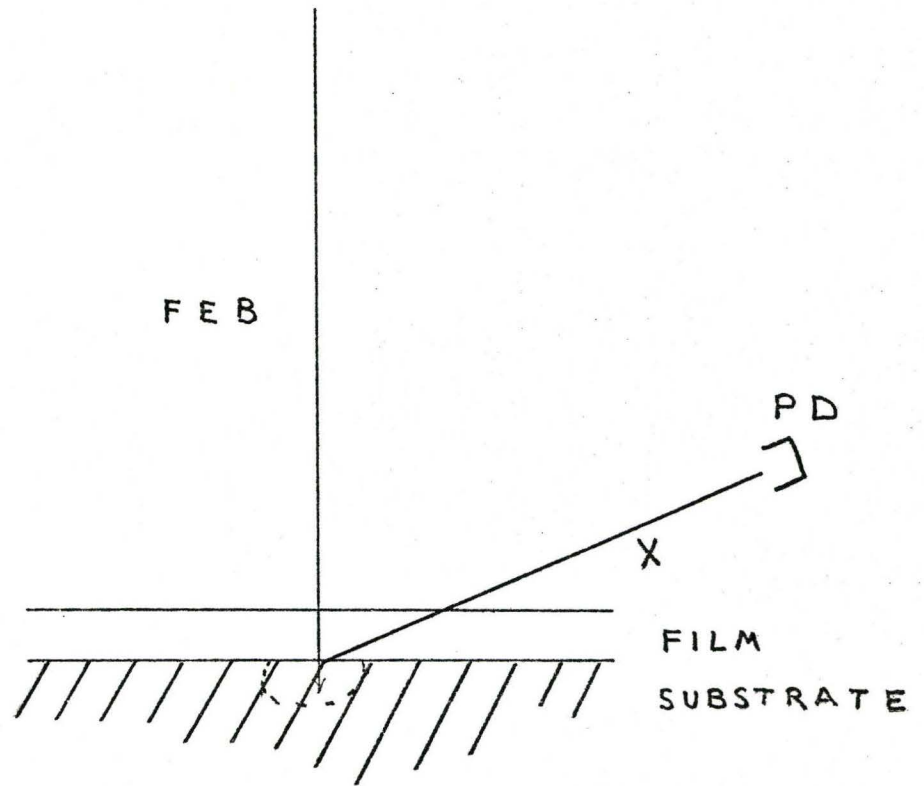


FIG. 19: PLOT FROM ELECTRON DIFFRACTION



FEB : FOCUSED ELECTRON BEAM

X : X - RAYS

PD : PROPORTIONAL DETECTOR

FIG. 20: ELECTRON MICROPROBE

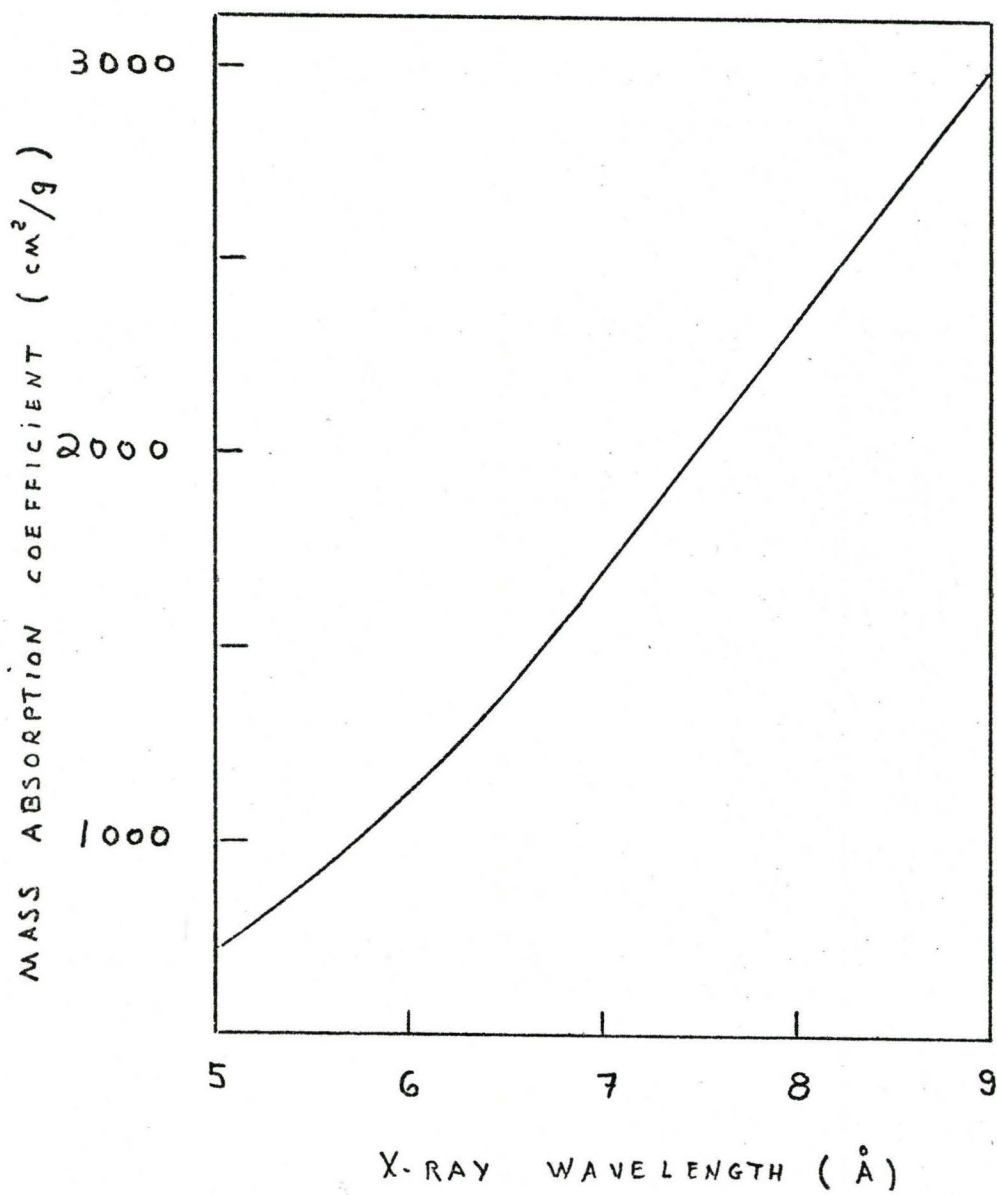


FIG. 21: MASS ABSORPTION COEFFICIENT OF VANADIUM

CHART SPEED 1 inch/min
SCAN SPEED 2.5 μ /sec
TIME SCALE 0.1 sec

CHART No. DS-107

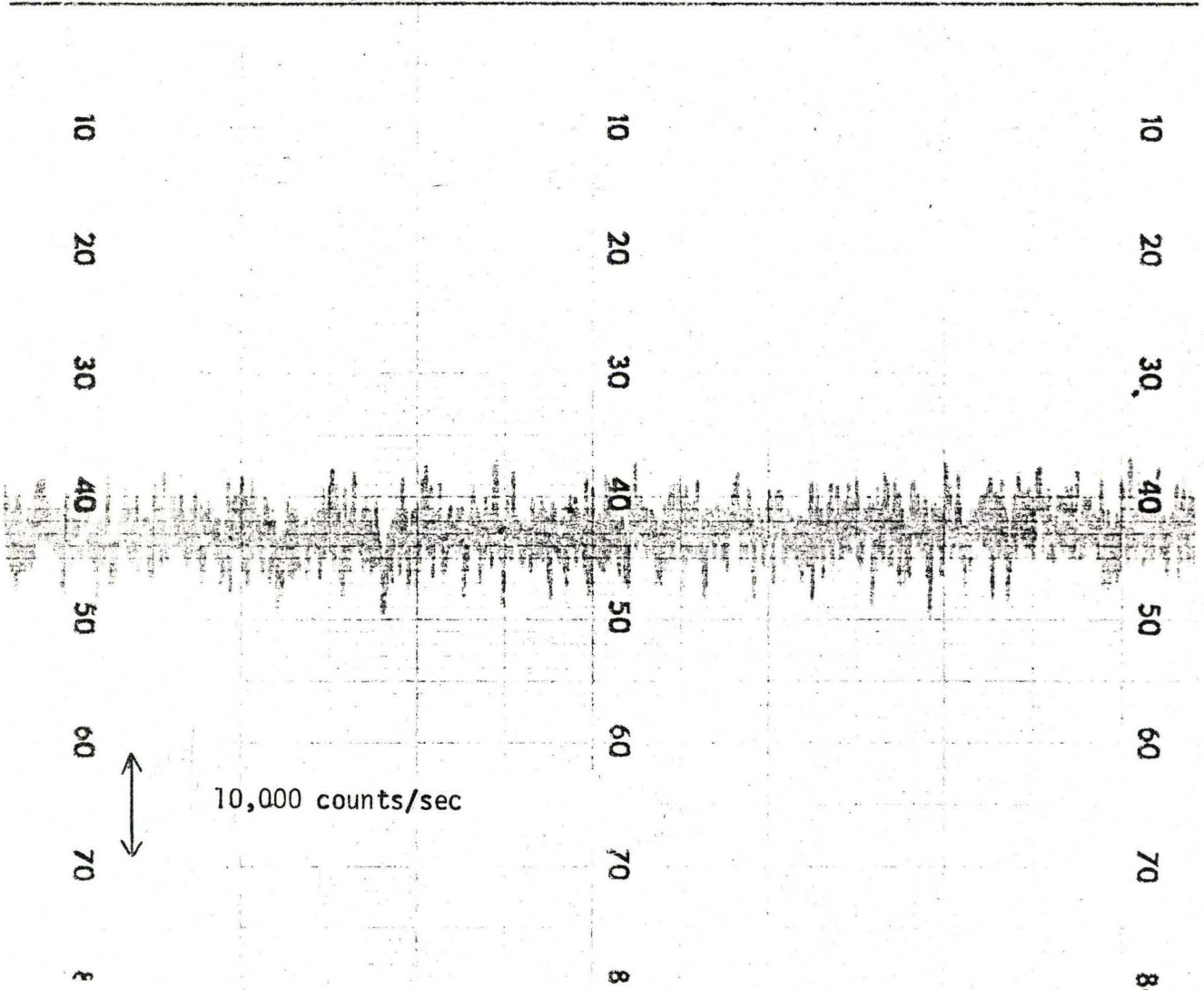


FIG. 22: CONTINUOUS PLOT OF INTENSITY OF X-RAYS ALONG THE FILM

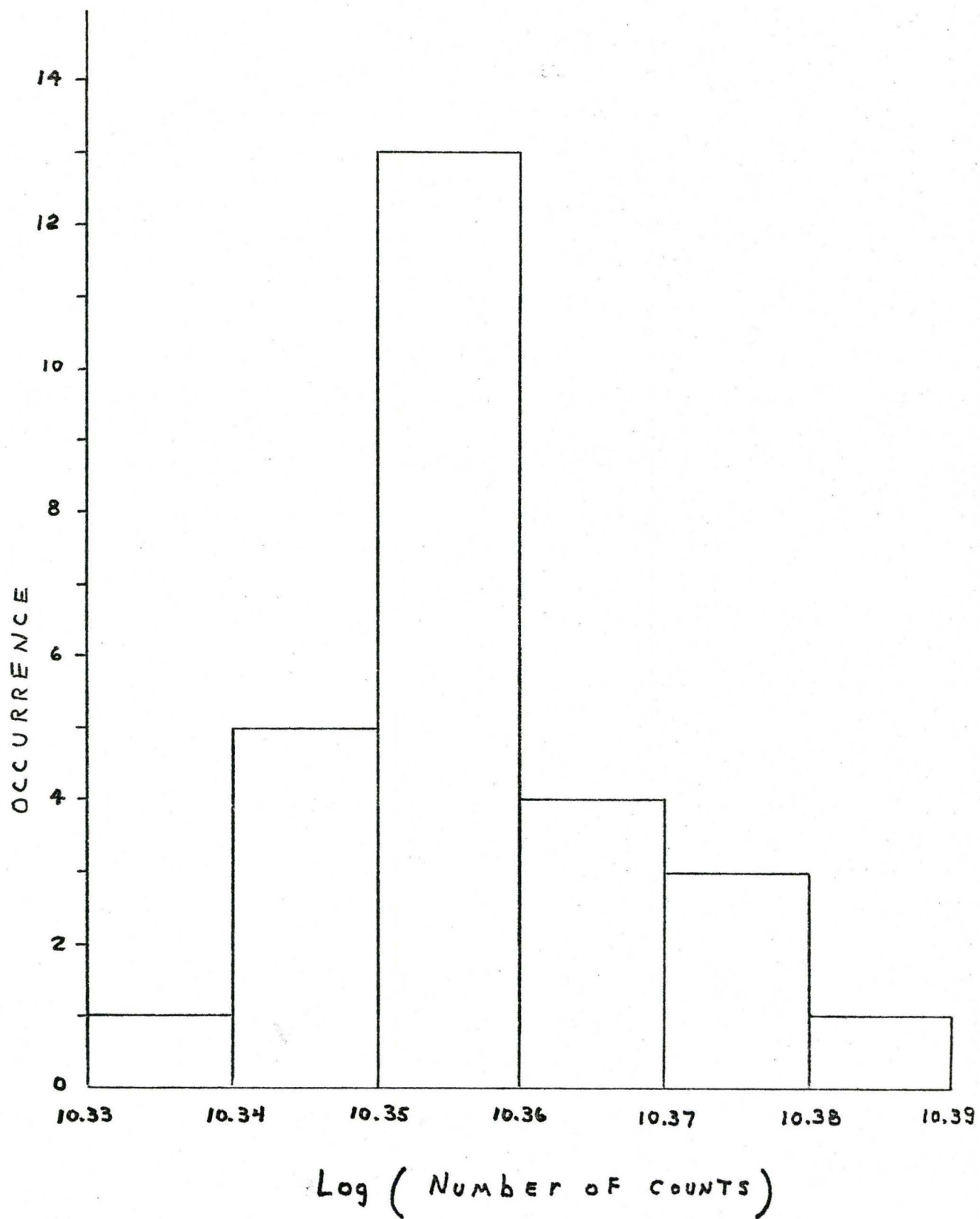


FIG. 23: INTENSITY DISTRIBUTION OF X-RAYS

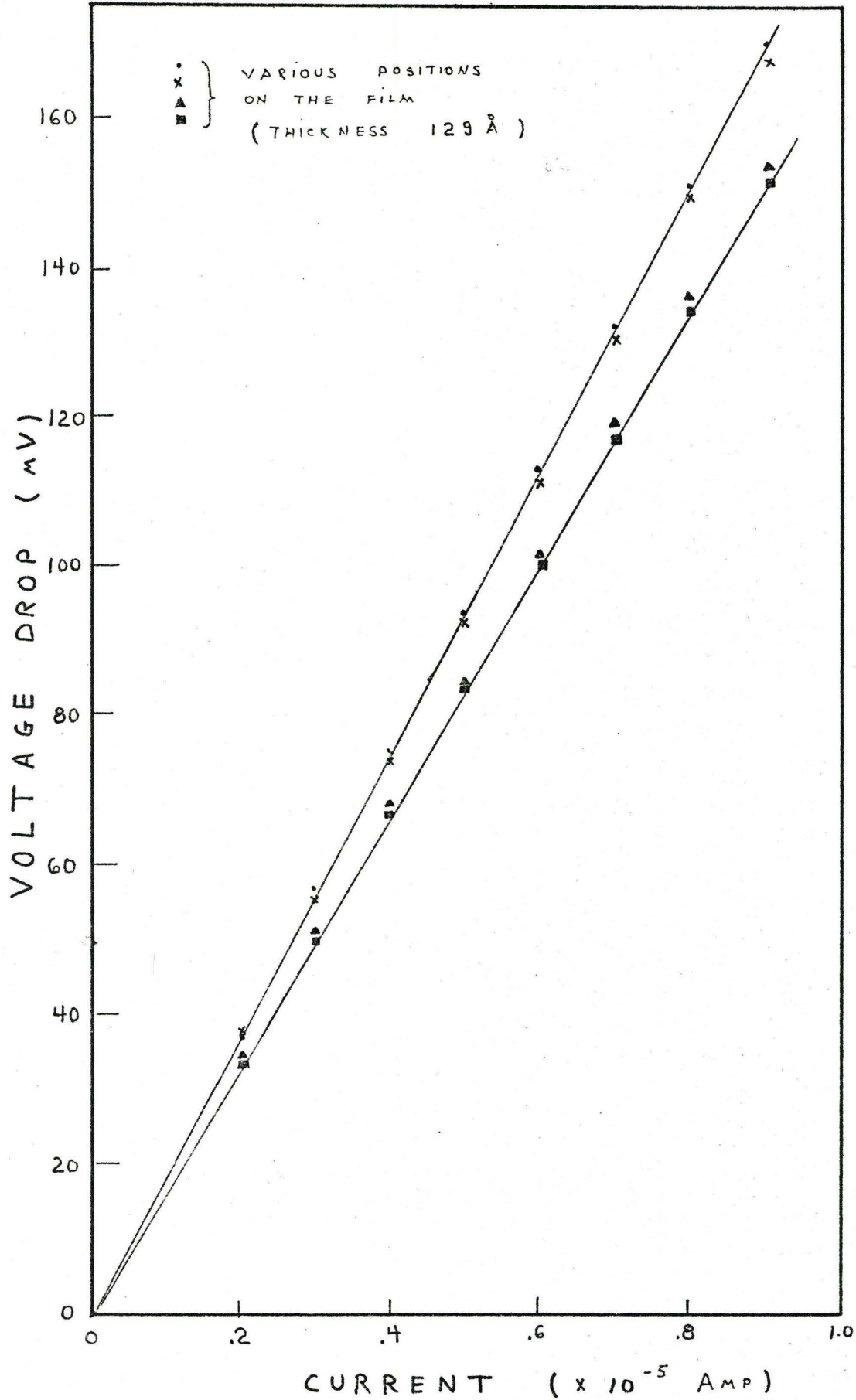


FIG. 24: V-I PLOT FOR RESISTIVITY

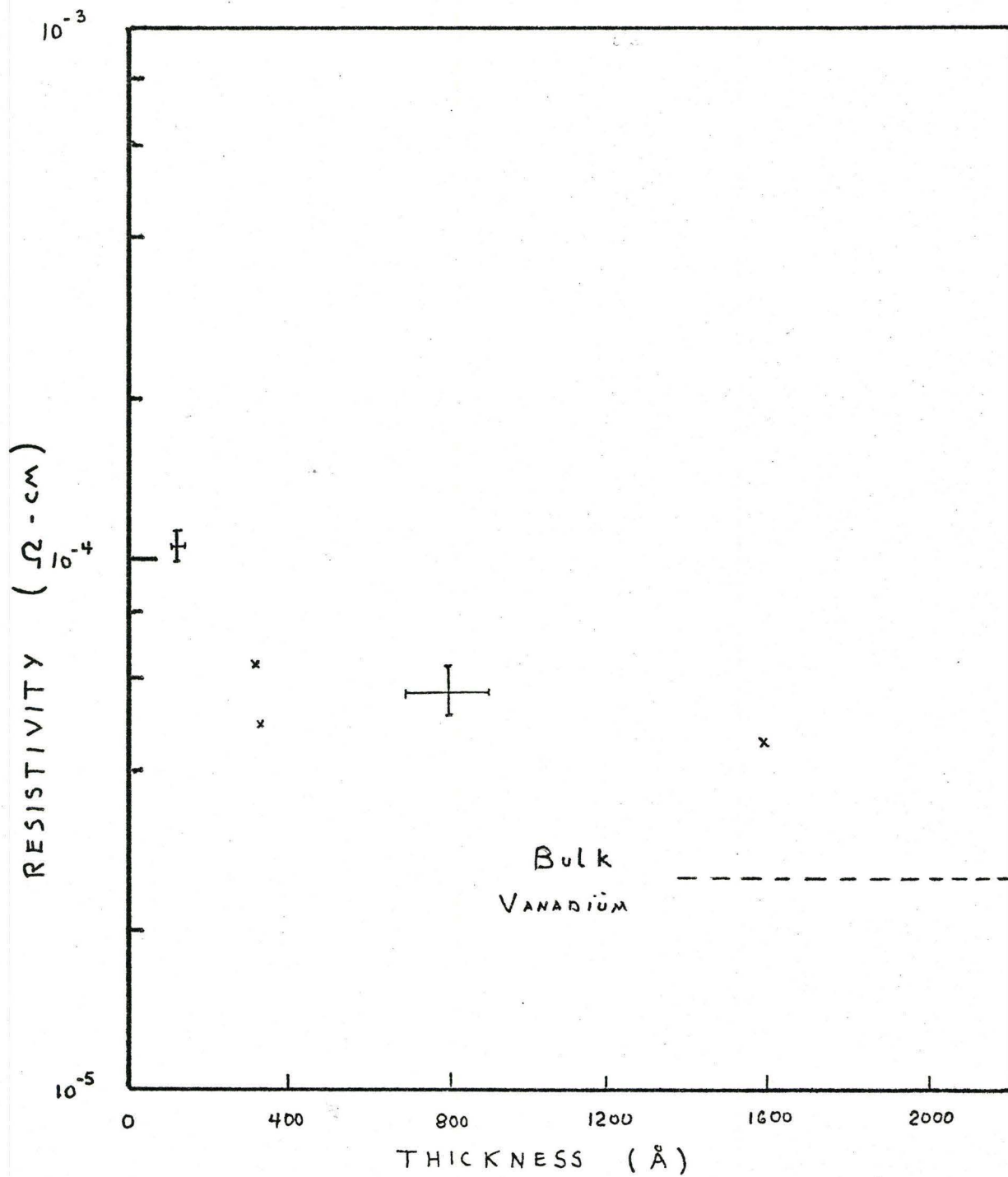


FIG. 25: RESULTS FROM RESISTIVITY MEASUREMENTS

TABLE I

EFFICIENCY OF ULTRASONIC CLEANING

Source	Coefficient of friction	
	Static (μ_s)	Kinetic (μ_k)
1 Mc/sec (300 W)	0.37	0.25
25 Kc/sec (125 W)	0.3	0.2

TABLE II

EFFICIENCY OF VARIOUS CLEANING PROCEDURES

METHOD	u_s	u_k	w(gr.)
1. Vapour degreasing in alcohol	0.5 - 0.64	0.4 - 0.62	30 - 40
2. Vapour degreasing in CCl_4	0.35	0.28	
3. Teepol washing and cloth drying	0.07	0.04	
4. Teepol washing cleaning in alcohol and wiping with cotton cloth	0.33	0.27	100
5. Precleaning with trichloreth and acetone. Concentration HNO_3 and washing in water			100
6. Teepol washing cleaning in alcohol and in chromic acid			100
7. Vapour degreasing and glow discharge cleaning	0.8	0.6	30 - 40
8. Teepol washing alcohol cleaning and flame drying	0.41		50
9. Vapour degreasing and vacuum melting			10

TABLE III

COMPARISON BETWEEN TWO SERIES OF MICROPHOTOGRAPHS SHOWING THE GROWTH OF Ag FILMS DEPOSITED AT LOW AND HIGH RATES (From L. Holland: "Vacuum Deposition of Thin Films" 1963).

2 A/min	20 A/min
Just before interconnection: Thickness is 220 A	Much more nuclei formed at first
Interconnection at 300 to 400 A	Equivalent thickness is 105 A
Channels start to fill up at 560 A	Interconnection at 100 A
	This stage at 120 A
	Perfectly smooth at 180 A

TABLE IV

ALLOWED (hkl) VALUES FOR DIAMOND FACE-CENTERED AND BODY-CENTERED CUBIC

Diamond		FCC		BCC		d_{hkl}
$h^2 + k^2 + l^2$ (hkl)		$h^2 + k^2 + l^2$ (hkl)		$h^2 + k^2 + l^2$ (hkl)		
				2	110	1.414
3	111	3	111			1.732
		4	200	4	200	2.000
				6	211	2.449
8	220	8	220	8	220	2.828
				10	310	3.162
11	311	11	311	11	311	3.317
		12	222	12	222	3.464
				14	321	3.742
16	400	16	400	16	400	4.000
				18	330	4.243
19	331	19	331			4.359
		20	420	20	420	4.472
				22	332	4.690
24	422	24	422	24	422	4.899
				26	431	5.099
27	333	27	333			5.196
				30	521	5.477
32	440	32	440	32	440	5.657

TABLE V

CHARACTERISTIC X-RAYS

Element	Film on Glass Slide	Bare Glass Slide	Empty Holder
Fe	Large amount	Large amount	Trace
Mn	None	None	None
Ni	Small amount (Average counting rate: 925 count/s)	Small amount (Average counting rate: 900 count/s)	None
Ti	Trace	Trace	None

TABLE VI

ELLIPSOMETRIC MEASUREMENTS

(a) Oxide Layer Thickness

Time elapsed in Air (Hrs.)	Thickness (A) Measured at different Angles of Incidence					
	60°		65°		70°	
1	37	1	39	1	41	1
12	40	1	43	1	45	1
113	44	1	48	1	50	1

(b) Film Thickness

Position	Average Thickness (A)
1	700
2	1200
3	1400
4	1200
5	2000

Variation along each line:

200 A

Crystal quartz thickness:

1723 A